NANO LETTERS

pubs.acs.org/NanoLett Letter

Friction and Adhesion Govern Yielding of Disordered Nanoparticle Packings: A Multiscale Adhesive Discrete Element Method Study

Xiaohui Liu,[∞] Joel A. Lefever,[∞] Daeyeon Lee, Jie Zhang, Robert W. Carpick,* and Ju Li*

Cite This: https://doi.org/10.1021/acs.nanolett.1c01952 Read Online

ACCESS | Metrics & More | Article Recommendations | Supporting Information

ABSTRACT: Recent studies have demonstrated that amorphous materials, from granular packings to atomic glasses, share multiple striking similarities, including a universal onset strain level for yield. This is despite vast differences in length scales and in the constituent particles' interactions. However, the nature of localized particle rearrangements is not well understood, and how local interactions affect overall performance remains unknown. Here, we introduce a multiscale adhesive discrete element method to simulate recent novel experiments of disordered nanoparticle packings indented and imaged with single nanoparticle resolution. The simulations exhibit multiple behaviors matching the experiments. By directly monitoring spatial rearrangements and interparticle bonding/debonding under the packing's surface, we uncover the mechanisms of the yielding and hardening phenomena observed in experiments. Interparticle friction and adhesion synergistically toughen the packings and retard plastic deformation. Moreover, plasticity can result from bond switching without particle rearrangements. These results furnish insights for understanding yielding in amorphous materials generally.

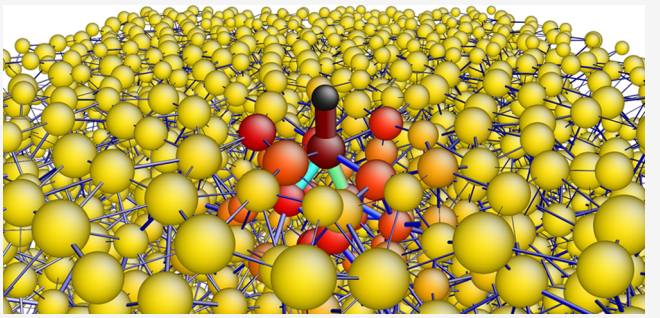

KEYWORDS: *Amorphous material, granular matter, discrete element simulation, nanoindentation, localized rearrangements, softness*

1. INTRODUCTION

The plasticity and flow of many classes of disordered packings have been investigated by experiments and simulations, including granular packings (typically with grains of >1 μm) such as sand,[1−3] pillars,[4−6] and disks[7,8] and those composed of smaller-scale constituents, including disordered nanoparticle packings (DNPs).[9−13] Studies have demonstrated that disordered packings across many size scales exhibit similar physics,[14] such as localized constituent particle rearrangements,[4] shear banding,[10] and brittle fracture.[13] Similar phenomena are also observed in many other amorphous materials, including metallic glasses[15−19] and colloidal glasses.[20,21] Despite these advances, the nature of these localized constituent-level rearrangements is still a rapidly developing area,[22] with many unanswered questions.

Interparticle friction is a prominent aspect of granular materials, which sets them apart from bubble rafts[23] and slowly deformed colloids,[20] and yields specific phenomena such as random loose packing,[24] shear jamming,[25,26] and anomalous diffusion.[1,2] Friction should affect the performance of DNPs as well,[11] though with nanoscopic friction laws that are possibly different from macroscopic laws.[27,28] It is of both scientific and engineering significance to investigate the effect of friction on the properties of disordered packings at various length scales. However, it is challenging in experiments to alter friction and thereby tune the resulting properties.

For grain sizes below ∼1 μm, it is also essential to address how interparticle adhesion affects the disordered packing's mechanical performance. This is because many DNPs with appealing functionality[29−37] have found only limited application owing to their poor mechanical reliability and durability,[10,38] wherein interparticle adhesion plays a critical role. While adhesion is known to impact certain aspects in adhesive disordered packings, such as the jamming phase diagram,[39] critical phenomena,[40] and the packing fraction,[41−43] to date, limited consideration has been given to how adhesion affects the mechanical response to external stimuli.

Among amorphous materials, DNPs are unique in that both friction and adhesion could be significant, making DNPs appropriate to serve as model materials to compare with other disordered systems, including granular matter and atomic glasses. In prior research, we investigated the plastic deformation of silica DNPs using atomic force microscopy (AFM)-based single-particle indentation.[11] Using high-resolution imaging and tracking, we succeeded in reproducibly

Received: May 27, 2021
Revised: September 16, 2021

Table 1. Key Parameters for the MADEM Indentation Simulations

parameter	default value[a]	range investigated	ref
number of particles	4000	N/A	N/A
particle diameter	20.0 ± 4.8 nm	polydisperse but not varied	11
packing size	≈370 × 370 × 200 nm^3	slightly varied depending on w	chosen to diminish the effect of the packing size
indenter radius	8 nm	6−16.7 nm	11
indentation velocity	0.1 m/s	0.01−1 m/s	limited by simulation time scale
sliding friction coefficient (μ_s)	0.3	0−0.6	28
work of adhesion (w)	109.62 mJ/m^2 (w_0)	(0−11) × w_0	52

[a]The default values are used in all simulations except for those where that parameter is tuned.

indenting on top of a *single* chosen nanoparticle in the packing. This stands in contrast to conventional nanoindentation experiments, where resolution at the individual particle level (i.e., atoms or molecules) is not achievable. It thus permitted us to (1) study the yielding of a disordered packing whose constituent particles are considered as "artificial atoms", i.e., as proxies for atoms in an amorphous material; the results validated that the behavior could be generalized and applied to understanding mechanisms of mechanical failure for disordered materials; and (2) learn about the behavior of these specific nanoparticle packings, whose application relevance is discussed above. From this, we argued that the results bear on amorphous material behavior in general. Specifically, we confirmed that yielding begins with localized rearrangements at the scale of a few particle diameters. This matches the proposed universal correlation length scale for rearrangement sizes observed on several disordered materials.[14]

However, the AFM method is not able to resolve particles located in the packing's interior, being restricted to imaging particles at the packing's surface. Thus, the underlying mechanisms of the mechanical responses could not be fully explored by the experiment itself.

Subsequently, we altered interparticle interactions by introducing water vapor into the system, leading to the formation of liquid bridges between nanoparticles via capillary condensation.[12] Nevertheless, it is difficult to quantitatively determine how capillary bridges affect adhesion forces at this nanometer length scale. Therefore, this method is not a perfect analog for tuning adhesion. In general, it is challenging to directly vary adhesion between the constituents of a disordered material experimentally, although some recent notable studies with granular[6] and colloidal[44] particles have succeeded in doing so.

Inspired by the unique experiments described above,[11,12] here we develop a novel multiscale adhesive discrete element method (MADEM) to simulate silica DNPs under single nanoparticle-level indentation. The MADEM simulations enable full resolution of each particle's position, with complete tunability of interparticle friction and adhesion along with many other desired parameters, which is challenging or impossible to accomplish experimentally. This allows exploration of how these factors modulate the packings' mechanical performance and provides insights potentially applicable to other disordered systems.

We demonstrate that there is strong heterogeneity in the particle-scale mechanical responses for the DNPs, with force-chain-like heterogeneous structures similar to those of macroscopic granular materials except that both friction and adhesion are crucial. We find that the interparticle normal contact and sliding frictional bonding and debonding play critical roles in governing yielding and hardening in the DNPs, even in the absence of particle rearrangements. This is a new paradigm for considering the nature of the unit processes involved in the plasticity of disordered materials. We also find a strong synergy between interparticle friction and adhesion in stabilizing and toughening the DNPs, which is not achieved in frictionless or nearly adhesionless packings.

2. METHODOLOGY

The traditional discrete element method (DEM)[45] has been extensively applied to investigate granular material behavior. To apply DEM to DNP simulations, one has to introduce interparticle adhesion. In MADEM, we describe the normal elastic interaction between deformable particles with adhesion via a multiscale adhesive contact model,[46] in which elastic contact is modeled within the framework of continuum mechanics involving large deformation, while interparticle adhesion is formulated by coarse-graining the interaction of molecules with neighboring particles using an intermolecular potential. This contact model is implemented within a nonlinear finite element formulation to simulate full-range contact processes between a spherical particle and a rigid plane to generate interparticle potentials with various effective radii. On the basis of these, we then develop a robust, efficient on-the-fly interpolation scheme to extract the adhesive normal contact force between particles with arbitrary effective radii, since our packings are polydisperse. Three other common modes of particle interaction due to friction (sliding, twisting, and rolling) are also incorporated in MADEM following previous work.[47−50] MADEM is implemented in the LAMMPS code;[51] detailed methodology is found in section I in Supporting Information.

To match the characteristics of the previously investigated alumina-coated silica DNPs,[11] 4000 particles with a uniform diameter distribution within 20.0 ± 4.8 nm are randomly generated within a box. In such a system, gravity may be ignored. The particles' elastic properties are taken to be those of amorphous silica, while the adhesion interaction is chosen to match the alumina coating. The default work of adhesion w_0 from van der Waals interactions between particles is obtained using the computed Hamaker constant of α-alumina[52] (see section II in Supporting Information for consideration of error introduced here). Some other types of interactions, like covalent or hydrogen bonding, could also be present in the experiments.[11] Thus, we vary the adhesion strength by boosting the work of adhesion w to be multiples of w_0 (see section III of Supporting Information for the sample preparation details). The packing fraction of the silica DNPs obtained is close to or above the random close packing limit[24] depending on w (section IV in Supporting Information).

Table 1 lists the key parameters used in the MADEM indentation simulations. The indenter is modeled as a sphere

https://doi.org/10.1021/acs.nanolett.1c01952
Nano Lett. XXXX, XXX, XXX−XXX

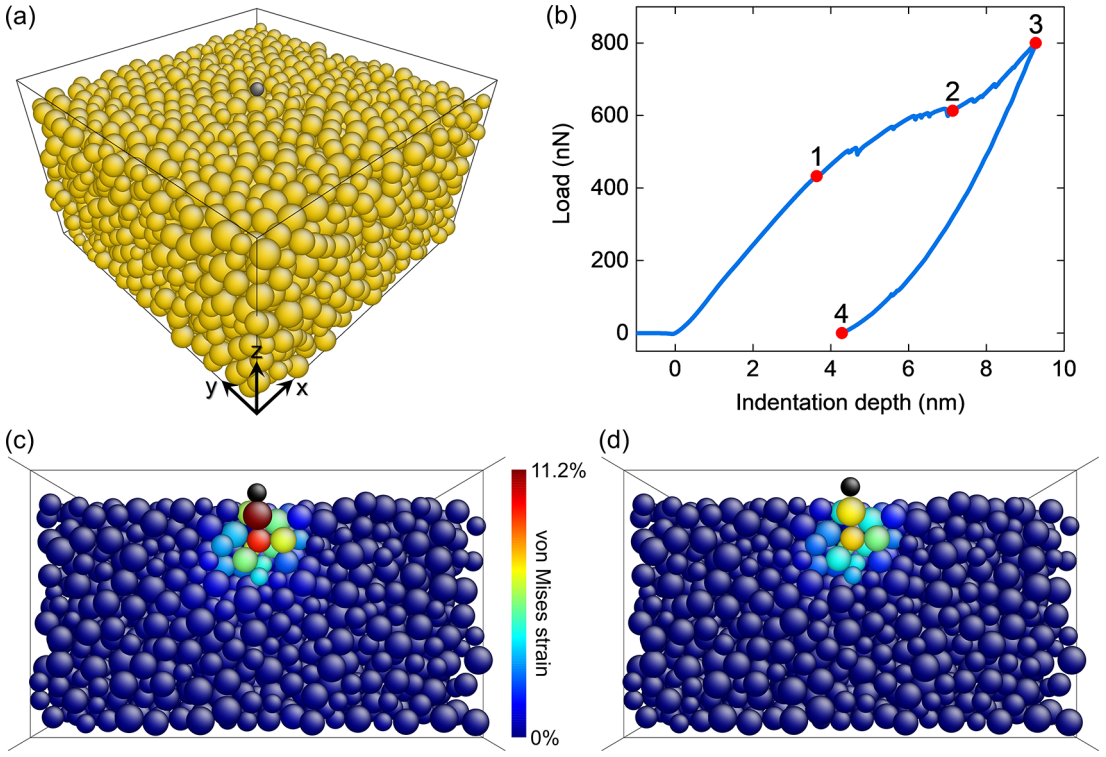

Figure 1. (a) Schematics of the configuration of a DNP for single-particle indentation simulation. (b) Typical simulated indentation load curve with $\mu_s = 0.3$, $w = 7w_0$ and the maximum load of 800 nN. (c) Cross-sectional view of the configuration at the maximum load corresponding to point 3 labeled in (b). (d) Configuration at the end of the indentation corresponding to point 4 labeled in (b). The size of the packing is about 370 × 370 × 200 nm^3, with periodic boundary conditions in the x and y directions, a silicon substrate on the bottom, and a free surface on the top. The black sphere denotes the indenter, with a radius of 8 nm. The particles are colored by their affine von Mises strain defined in ref 53 as measured relative to their initial positions, visualized by AtomEye.[54] See Supporting Information Movie S1 for the full evolution of the packing configuration over the course of indentation.

with mechanical properties matching that of diamond to mimic the spherical tip of the hard, tetrahedral amorphous carbon AFM probe used in experiments.[11] The effects of the indenter size and the indentation velocity on the indentation load are presented in sections V and VI in Supporting Information, respectively. We also tune the sliding friction coefficient μ_s and work of adhesion w between particles to investigate their effects on the DNP's mechanical response, as discussed below.

3. RESULTS AND DISCUSSION

A typical simulated indentation load curve and the packing configurations illustrating the deformation under the applied load are shown in Figure 1 and Supporting Information Movie S1. Following the experiments,[11] the simulation is run until a load of 800 nN is reached, and then the indenter is withdrawn. The strain remaining after the indentation demonstrates that plastic deformation has occurred. The majority of plastic deformation is limited to a region a few particles in size beneath the indenter, and there is almost no strain near the lateral boundaries and the substrate over the course of indentation, implying a fairly weak boundary effect.

Multiple specific phenomena from experiments are reproduced well. Figure 2a shows the load curves resulting from indentation simulations performed at various locations on the DNP film. Substantial differences are apparent including a large variation in the indentation depth, indicating that the local mechanical properties vary spatially across the film. Deeper indents correspond to greater energy dissipation. Specifically, load curves corresponding to deeper indentation depths also enclose a larger area with a greater residual indentation depth after unloading, implying that a locally soft region is where more plastic deformation occurs and not simply more elastic compliance. Figure 2b shows simulated load curves obtained by repeated indentation at the same location. The hysteresis in each curve indicates that energy is lost due to dissipative mechanisms, which are explained further below. These results compare favorably with Figure 5 of ref 11 (as reproduced in Figure 2c,d here), particularly regarding the indentation depths and elastic moduli. For instance, we observe a similar range of indentation depths at randomly selected locations, in the range of 6.0−13.6 nm in simulations (Figure 2a) and 3.4−12.5 nm in experiments (Figure 2c). Also, the substantial plastic deformation on the initial indent followed by nearly pure elastic deformation in subsequent indents (Figure 2b) closely matches the previous experimental results (Figure 2d).

Simulation results demonstrate that the most significant form of energy dissipation is the sliding friction between the particles, in both the first indent cycle and the subsequent cycles in Figure 2b, as shown in Figure 3. In addition to the dissipated plastic energy, some energy is also stored elastically in the form of adhesive normal contact strain and sliding/twisting/rolling elastic strains at particle interfaces. Not all the elastic energy is recovered when the load is withdrawn due to strain energy stored in these interparticle bonds. Kinetic energy accounts for only a small portion of the total energy, supporting the treatment of DNP indentation as a quasi-static process. Similar to the previous experiments,[11] the character-

https://doi.org/10.1021/acs.nanolett.1c01952
Nano Lett. XXXX, XXX, XXX−XXX

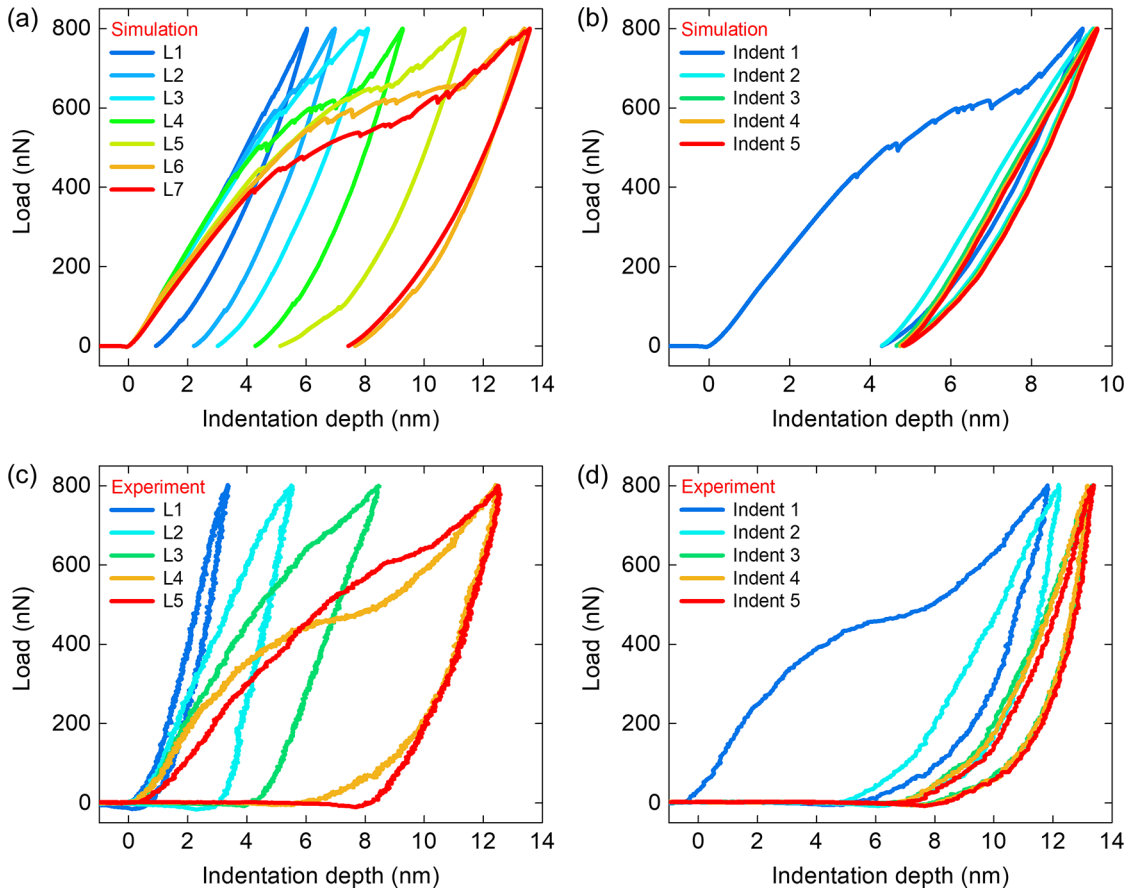

Figure 2. (a) Simulated load curves for seven different locations indented on the packing given in Figure 1. (b) Simulated load curves of a series of five repeated indents performed at a single location on the packing. For comparison, Figure 5a and Figure 5b from ref 11 are reproduced as (c) and (d) here, showing the experimental results of the load curves for different locations and for repeated indents at a single location, respectively. All the curves have the maximum load of 800 nN. Note that the samples for the simulations are not guaranteed to have particles with the same position and size as those for the experiments, since we lack the information about the particles within the interior of the latter due to the limitation of AFM.

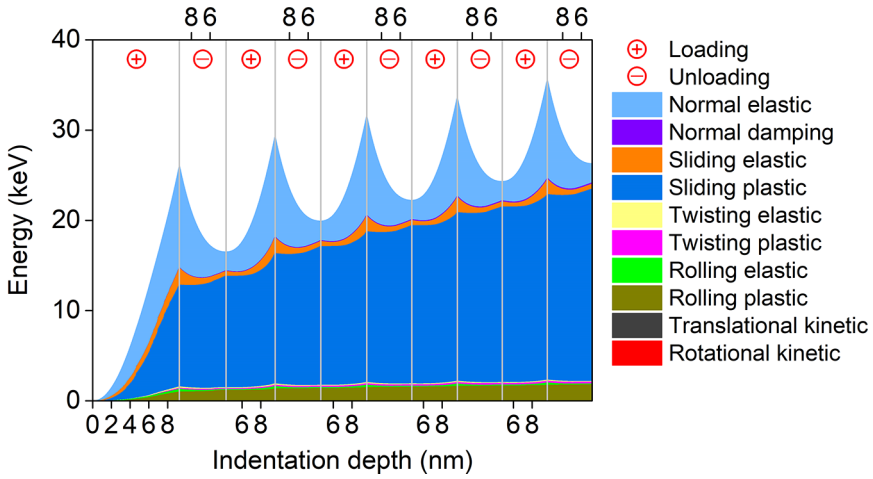

Figure 3. Evolution of the energy accumulated and dissipated in the packing over the course of five complete indent cycles repeated at the same location, corresponding to Figure 2b. The sliding/twisting/rolling elastic energy denotes the energy stored elastically owing to static friction between particles, while the sliding/twisting/rolling plastic energy denotes that dissipated owing to kinetic friction between particles. The amount of the translational/kinetic energy is too small to be visible in the figure. The formulas for the energy calculation are listed in Table S3 in Supporting Information.

istic energy magnitude is on the order of tens of keV, which is mainly shared among tens of particles positioned locally beneath the indenter. This demonstrates that our packing system can be treated as athermal. In this regard, thermal activation, which is usually omitted in granular matter, should play a negligible role as well in our DNPs.

In prior experiments,[11] an inflection is frequently observed in the indentation load curves with deep indents, as shown in

https://doi.org/10.1021/acs.nanolett.1c01952
Nano Lett. XXXX, XXX, XXX−XXX

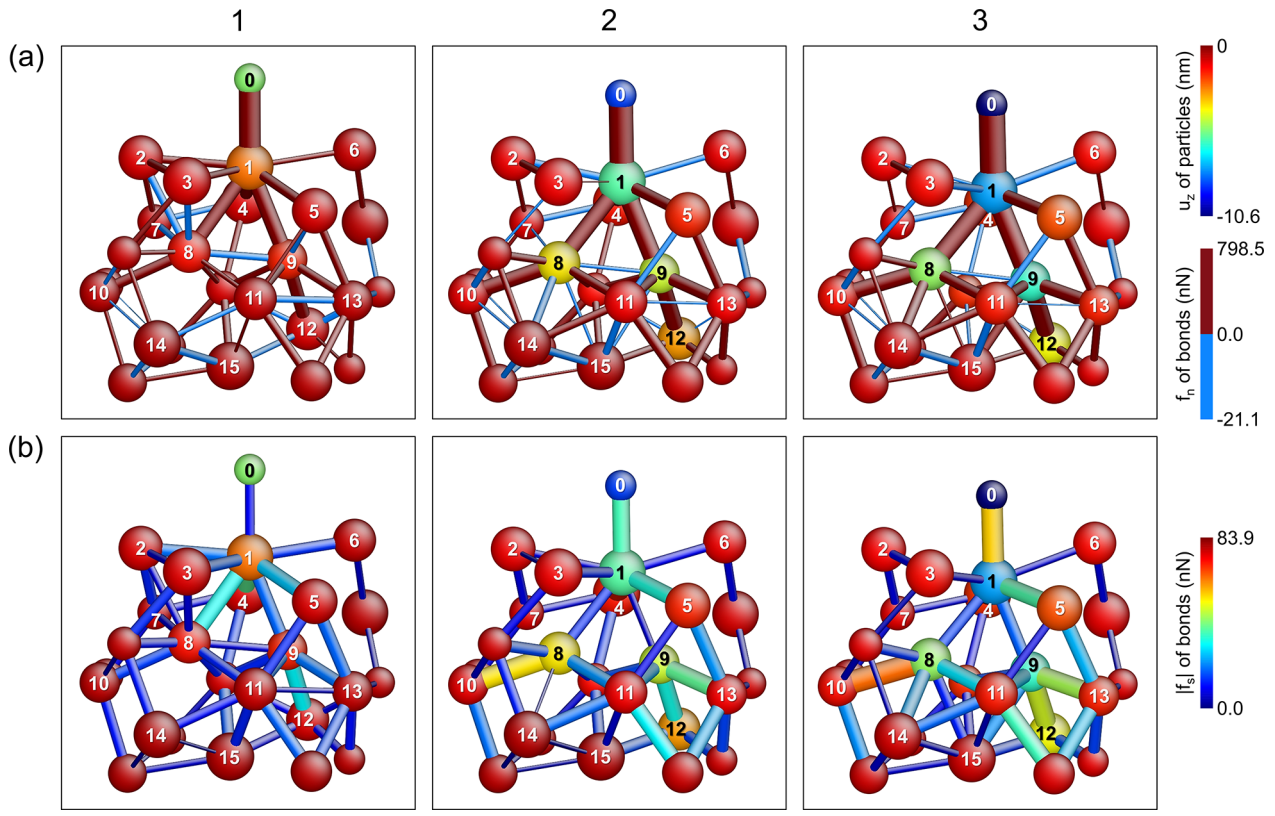

Figure 4. Snapshots of the local configuration under the indenter with the numerical labels 1−3 on the top corresponding to the points labeled in Figure 1b. The indenter is labeled as 0. (a) The bonds display the interparticle normal contact force (f_n) chains, with repulsive (positive) and attractive (negative) f_n colored by red and blue, respectively. This binary color scheme is chosen to make the bonds with repulsion and attraction more distinguishable. (b) Here, the bonds display the sliding frictional force (f_s) chains, colored according to the magnitude of f_s. In (a) and (b), the bond size reflects the magnitude of the respective interparticle force, with the bond radii scaled proportional to $|f_n|^{1/3}$ (or $|f_s|^{1/2}$) rather than $|f_n|$ (or $|f_s|$) in order to make the bonds with small $|f_n|$ (or $|f_s|$) more visible. The particles themselves are colored by their z-displacement u_z and have been scaled down to make the bonds visible. See Supporting Information Movie S2 for the full evolution of the f_n and f_s chains over the course of indentation. Detailed conditions for the formation and breakage of the bonds can be found in section I of Supporting Information.

Figure 2c (L4 and L5) and Figure 2d (indent 1). This indicates that the packing undergoes plastic yielding and hardening before and after the inflection. However, the mechanisms of the yielding and hardening remained elusive because the AFM cannot explore the packing's interior. Our simulations reproduce these phenomena well (Figure 2a,b), enabling us to peer into the configurational evolution and analyze the interparticle interactions. Figure 4 shows the local topologies under the indenter as well as the truss-like normal contact force chains and the sliding frictional force chains corresponding to the time points 1−3 labeled in Figure 1b, which correspond to before initial yielding, after initial yielding (at the inflection point), and within the hardening stage, respectively. Since only particle 1 bridges the indenter (labeled as particle 0), its motion, due to the interactions with all its neighbors, immediately influences the indentation load. Surface particles 2−6 impose most of the frictional resistance to particle 1 along the z direction (Figure 4b), while particles 8 and 9, which are the closest subsurface particles to particle 1, carry much of the normal force to balance particle 1 from below (Figure 4a). Before yielding, particles 2 and 3 exert attractive forces on particle 8 as a result of adhesion (Figure 4a-1), but these two bonds are broken afterward (Figure 4a-2) as particle 8 is constantly driven by particle 1 from above. Moreover, particle 8 is further attracted by particles 14 and 15 from below by forming new bonding. Almost simultaneously, particle 9 loses the bond with attractive force from particle 5. These drive particles 8 and 9 to accelerate to move downward with conspicuous z-displacements, as shown in Figure 4a-2, which relaxes the repulsive force acting on particle 1. This change of the force chains greatly affects the trajectory of particle 1 thereafter and also the load transmitted to the indenter, then followed by yielding. The above analysis demonstrates that the plastic deformation is the result of bond switching without significant local rearrangements below the indenter. This bond switching phenomenon is frequently observed in our simulations and is seen explicitly in Supporting Information Movie S2.

The hardening mechanism can also be revealed by analysis of the bonding evolution. Under further indentation, particle 9 gains stronger support from particle 12, and the normal contact forces of the bonds 8−14 and 8−15 change from attraction to repulsion, which contributes to supporting particle 8 from below (Figure 4a-3). In the meantime, as shown in Figure 4b-3, particle 8 is subjected to stronger frictional forces by its neighboring particles 10, 11, and 14, as does particle 9 by particles 11 and 13. These particles resist the downward motion of particle 1 and the indenter, which is responsible for the ensuing hardening. In experiments,[11] the larger AFM tip had more chance to collide with the surface particles, which could also contribute to the hardening and has been validated by our simulations (see section V in Supporting Information).

https://doi.org/10.1021/acs.nanolett.1c01952
Nano Lett. XXXX, XXX, XXX−XXX

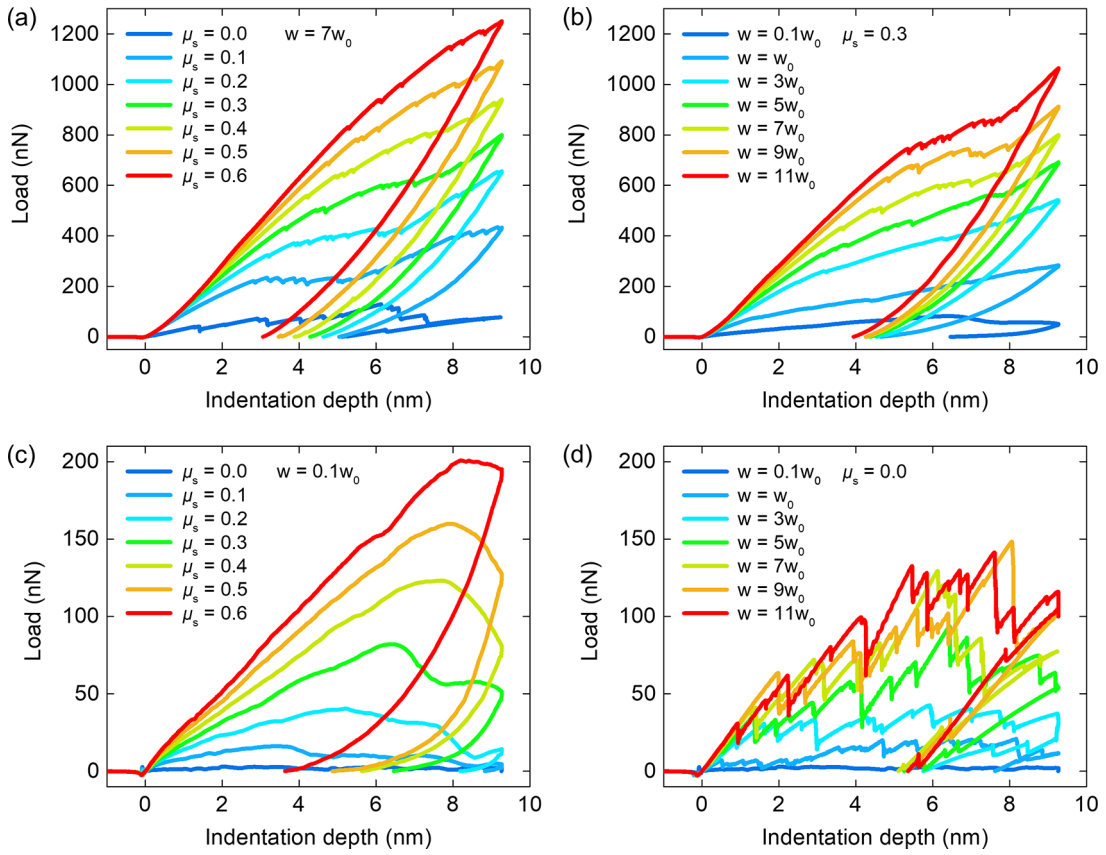

Figure 5. Simulated indentation load curves with various μ_s while keeping (a) $w = 7w_0$ and (c) $w = 0.1w_0$, and with various w while keeping (b) $\mu_s = 0.3$ and (d) $\mu_s = 0$. We choose to investigate the packings with weak adhesion in (c) instead of purely adhesionless ones ($w = 0$), as the latter lose their original marginal rigidity states and disassemble under the perturbation by indentation. All the simulations in (a) and (c) are performed using the same initial packing configuration and at the same indent location, respectively. The initial packing configurations with different w used in (b) and (d) share a certain similarity in topology, respectively (see section III in Supporting Information for the protocols for preparing the packings), and all the simulations are performed at the indent location right above the same surface particle in each packing. For comparison, all the curves in (a)−(d) have the same maximum indentation depth as that in Figure 1b, which is 9.27 nm. Note the greatly reduced load scale in (c) and (d).

These two hardening mechanisms above can be differentiated by using a smaller indenter as in our simulations.

The effects of friction and adhesion on the mechanical response of the DNPs under indentation are investigated by either changing μ_s or w, as shown in Figure 5. The structural stability of the DNPs is remarkably improved by the introduction of both friction and adhesion (Figure 5a,b) as compared to the nearly adhesionless (Figure 5c) and frictionless (Figure 5d) systems. Furthermore, increasing either μ_s (Figure 5a) or w (Figure 5b) can enhance the loading stiffness of the packings in the presence of both friction and adhesion, though the underlying mechanisms are different in these two cases. The projection of the frictional tangential forces in the normal direction can compensate for the normal contact forces between particles and prevent the breaking of contacts,[55] thus making the packings stiffer. In contrast, stronger adhesion yields shorter equilibrium interparticle separations naturally, which brings about a higher elastic modulus of the packings as well. With regard to unloading, friction plays a much less important role, especially in the early stage of retraction, as evidenced by the drastic drop of the sliding plastic power dissipation shown in Figure S12 in Supporting Information. Accordingly, unloading largely reflects the intrinsic elasticity of the packing, which is quite dependent on the adhesion strength. This can explain why the initial unloading stiffness, which determines the indentation modulus,[56] is fairly sensitive to the change of w (Figure 5b) but not to μ_s except for very small μ_s (Figure 5a). Another observation from Figure 5a,b is that either friction or adhesion can delay the onset of yielding, signifying a higher energy barrier to be surmounted for plastic deformation. However, plastic deformation cannot be eliminated even if we greatly increase μ_s or w. This indicates that the local plasticity or softness is decided by both the local structure and energetics.[57,58]

The simulation results in Figure 5 also demonstrate that friction and adhesion synergistically stabilize and toughen the DNPs to a great extent. Note that friction itself is able to endow only limited mechanical strength in the case of weak adhesion ($w = 0.1w_0$, Figure 5c). Higher friction yields somewhat higher strength but is still far less effective at strengthening a DNP than tightened by the adhesive force (Figure 5a). We ascertain that the indentation load drops shown in Figure 5c correspond to structural instabilities resulting in pile-up on the packings' surface due to the shear dilatancy effect[59] induced by the indentation (see Supporting Information Movie S3). This effect is suppressed when adhesion is enhanced (Figure 5a and Supporting Information Movie S1), since the adhesive force makes dilatancy harder.

The adhesive but frictionless packings (Figure 5d) do gain enhanced stiffness in the case of stronger adhesion; however, they remain structurally unstable as evidenced by the precipitous serrations on the load curves. Each serration

https://doi.org/10.1021/acs.nanolett.1c01952
Nano Lett. XXXX, XXX, XXX−XXX

corresponds to softening or breaking of one or more interparticle bonds (Supporting Information Movie S4), which is attributed to the external force separating two particles exceeding their pull-off force, i.e., the negative of the minimum of the normal elastic contact force between them. Consequently, it will suddenly break the force balance of the global normal contact force chains, which may lead to a structural rearrangement. Generally, higher w results in a larger pull-off force and a larger rearrangement, which limits the attainable mechanical strength of the packings with strong adhesion but no friction.

However, this situation can be significantly alleviated by introducing friction (Figure 5b), since friction offers shearing resistance and effectively mitigates particle rearrangements, thus improving toughness. As well, stronger adhesion strengthens the frictional forces. Unlike in an atomic glass, in which the interatomic potential energy released by atomic rearrangements is converted into kinetic energy, in a DNP the interparticle potential energy of normal contact released during plastic deformation is mainly dissipated by friction rather than particle vibrations (see Figure S12 in Supporting Information). In this regard, friction enhances the ability of the packing to absorb energy and hinders further exploration in configurational space to relax strain energy. This also suggests interparticle friction as a mechanism for improving the mechanical stability and toughness of disordered materials. Moreover, the adhesive force can be strengthened by shortening the interparticle separation with the aid of the tangential frictional force, which retards the debonding of particles and thus further enhances toughness. The interplay of friction and adhesion revealed here suggests possibly establishing a more general jamming phase diagram, which could incorporate those for frictional particles[25] and for attractive particles,[39,60,61] generalizing Liu and Nagel's original jamming phase diagram.[62]

4. CONCLUSION

We have developed the MADEM approach, which can handle packings consisting of polydisperse frictional and adhesive particles undergoing large deformation. MADEM can straightforwardly deal with macroscopic granular systems by simply ignoring the interparticle adhesion and can also be conveniently extended to simulate colloidal systems by applying additional Stokes' drag force and stochastic force on particles.

We have modeled recent unique indentation experiments conducted on DNPs with single nanoparticle resolution. By performing MADEM simulations, we have reproduced multiple attributes of the DNPs that match previous experiments. This includes substantial particle-level spatial heterogeneity in stiffness, energy dissipation, and the amount of plasticity. This agreement is attained when using a value of adhesion several times greater than the van der Waals adhesion value for the nanoparticles, suggesting that stronger bonding mechanisms such as covalent bonds, hydrogen bonds, or capillary forces[12] were present in the experiments. We have also shown that thermal activation can be omitted in our DNPs wherein strong dissipation exists, despite the fact that the constituent particles are nanoscale in size.

Furthermore, we uncover the mechanisms of the localized yielding and hardening phenomena observed in both experiments and simulations, where switching of the interparticle bonding plays a critical role. This demonstrates that signatures of plasticity in this system, and perhaps others, can involve changes in the magnitude and sign of interparticle interaction forces in the absence of particle rearrangements. This adds a new dimension to the theory of how plasticity initiates in disordered systems. We further demonstrate that a strong interplay between friction and adhesion is crucial to retard plastic deformation and give rise to enhanced structural stability and toughness of the DNPs. This deepens the understanding of the roles of friction and adhesion in regulating the deformation of DNPs and may furnish possible guidance for designing DNPs with better mechanical performance.

This work helps to establish connections between the physics of DNPs and other amorphous systems. For example, atomic glasses with covalent bonding may feature similarly enhanced stiffness compared to more isotropically bonded systems, since the directional nature of covalent bonds provides an angular resistance, which bears a certain resemblance to interparticle friction. Any atomic glass, regardless of bonding type, is expected to behave similarly in some aspects to DNPs, as attractive forces are present in both cases. Moreover, DNPs should share similar behavior with many geological systems,[63] where friction and adhesion are of key importance as well, such as the pressure sensitivity and flow non-normality in the yield surface.[64,65] For instance, the strong dependence of the indentation load on adhesion in the presence of friction that we report (Figure 5b) is indicative of the pressure sensitivity of the yielding, since adhesion acts like a confining pressure in jamming systems.[39] In general, the current simulations provide a means by which the similarities and differences between atomic glasses and larger-scale granular matter may be explored, in particular by varying the bonding potential, mass, and length scale.

■ ASSOCIATED CONTENT

Supporting Information

The Supporting Information is available free of charge at https://pubs.acs.org/doi/10.1021/acs.nanolett.1c01952.

Introduction of the MADEM we develop; error analysis of the adhesive force between a coated sphere and a semi-infinite plane; protocols for preparing nanoparticle packings for indentation simulations and packing fraction calculation; effect of the work of adhesion on packing fraction; effect of the indenter size on mechanical response; effect of the indentation velocity on mechanical response; a supporting table listing the formulas for the energy calculation listed in Figure 3; a supporting figure displaying the evolution of the power of the normal elastic energy and the sliding plastic energy for the curve with $\mu_s = 0.3$ and $w = 7w_0$ shown in Figure 5 (PDF)

Movie S1 showing the evolution of the packing configuration over the course of the indentation corresponding to Figure 1 (AVI)

Movie S2 showing the evolution of the interparticle normal contact force chains and the sliding frictional force chains corresponding to Figure 4 (AVI)

Movie S3 showing the evolution of the packing configuration with $\mu_s = 0.3$ and $w = 0.1w_0$ (AVI)

Movie S4 showing the evolution of the interparticle normal contact force chains of the packing with $\mu_s = 0$ and $w = 7w_0$ (AVI)

https://doi.org/10.1021/acs.nanolett.1c01952
Nano Lett. XXXX, XXX, XXX−XXX

AUTHOR INFORMATION

Corresponding Authors

Robert W. Carpick − *Department of Mechanical Engineering and Applied Mechanics, University of Pennsylvania, Philadelphia, Pennsylvania 19104, United States;* orcid.org/0000-0002-3235-3156; Email: carpick@seas.upenn.edu

Ju Li − *Department of Nuclear Science and Engineering, Massachusetts Institute of Technology, Cambridge, Massachusetts 02139, United States; Department of Materials Science and Engineering, Massachusetts Institute of Technology, Cambridge, Massachusetts 02139, United States;* orcid.org/0000-0002-7841-8058; Email: liju@mit.edu

Authors

Xiaohui Liu − *Institute of Materials Modification and Modeling, School of Materials Science and Engineering, Shanghai Jiao Tong University, Shanghai 200240, China; Materials Genome Initiative Center, Shanghai Jiao Tong University, Shanghai 200240, China; Department of Nuclear Science and Engineering, Massachusetts Institute of Technology, Cambridge, Massachusetts 02139, United States;* orcid.org/0000-0003-1598-0657

Joel A. Lefever − *Department of Materials Science and Engineering, University of Pennsylvania, Philadelphia, Pennsylvania 19104, United States;* Present Address: Asylum Research—An Oxford Instruments Company, Santa Barbara, CA 93117, United States

Daeyeon Lee − *Department of Chemical and Biomolecular Engineering, University of Pennsylvania, Philadelphia, Pennsylvania 19104, United States;* orcid.org/0000-0001-6679-290X

Jie Zhang − *Institute of Natural Sciences and School of Physics and Astronomy, Shanghai Jiao Tong University, Shanghai 200240, China*

Complete contact information is available at: https://pubs.acs.org/10.1021/acs.nanolett.1c01952

Author Contributions

[∞]X.L. and J.A.L. contributed equally.

Notes

The authors declare no competing financial interest.

ACKNOWLEDGMENTS

X.L. acknowledges support by the China Scholarship Council (Grant 201406235041) and is thankful for helpful discussions with Dr. Wenbin Li and Dr. Yunwei Mao. J.A.L. acknowledges support from the Ashton Foundation. This research was partially supported by NSF through the University of Pennsylvania Materials Research Science and Engineering Center (MRSEC) (DMR-1720530) (R.W.C., D.L. and J.A.L.). R.W.C. also acknowledges support from Grant NSF DMR-1120901. J.L. acknowledges support by Grant NSF DMR-1923976. This work was carried out in part at the Singh Center for Nanotechnology, which is supported by the NSF National Nanotechnology Coordinated Infrastructure Program under Grant NNCI-2025608.

REFERENCES

(1) Royer, J. R.; Chaikin, P. M. Precisely cyclic sand: self-organization of periodically sheared frictional grains. *Proc. Natl. Acad. Sci. U. S. A.* **2015**, *112*, 49−53.

(2) Kou, B.; et al. Granular materials flow like complex fluids. *Nature* **2017**, *551*, 360−363.

(3) Xing, Y.; et al. X-ray Tomography investigation of cyclically sheared granular materials. *Phys. Rev. Lett.* **2021**, *126*, 048002.

(4) Cubuk, E. D.; et al. Identifying structural flow defects in disordered solids using Machine-learning Methods. *Phys. Rev. Lett.* **2015**, *114*, 108001.

(5) Li, W.; Rieser, J. M.; Liu, A. J.; Durian, D. J.; Li, J. Deformation-driven diffusion and plastic flow in amorphous granular pillars. *Phys. Rev. E* **2015**, *91*, 062212.

(6) Rieser, J. M.; Arratia, P. E.; Yodh, A. G.; Gollub, J. P.; Durian, D. J. Tunable capillary-induced attraction between vertical cylinders. *Langmuir* **2015**, *31*, 2421−2429.

(7) Utter, B.; Behringer, R. Experimental measures of affine and nonaffine deformation in granular shear. *Phys. Rev. Lett.* **2008**, *100*, 208302.

(8) Wang, Y.; Wang, Y.; Zhang, J. Connecting shear localization with the long-range correlated polarized stress fields in granular materials. *Nat. Commun.* **2020**, *11*, 4349.

(9) Zhang, L.; Prosser, J. H.; Feng, G.; Lee, D. Mechanical properties of atomic layer deposition-reinforced nanoparticle thin films. *Nanoscale* **2012**, *4*, 6543−6552.

(10) Zhang, L.; et al. Using shape anisotropy to toughen disordered nanoparticle assemblies. *ACS Nano* **2013**, *7*, 8043−8050.

(11) Lefever, J. A.; et al. Heterogeneity in the small-scale deformation behavior of disordered nanoparticle packings. *Nano Lett.* **2016**, *16*, 2455−2462.

(12) Lefever, J. A.; Mulderrig, J. P.; Hor, J. L.; Lee, D.; Carpick, R. W. Disordered nanoparticle packings under local stress exhibit avalanche-like, environmentally dependent plastic deformation. *Nano Lett.* **2018**, *18*, 5418−5425.

(13) An, L.; Zhang, D.; Zhang, L.; Feng, G. Effect of nanoparticle size on the mechanical properties of nanoparticle assemblies. *Nanoscale* **2019**, *11*, 9563−9573.

(14) Cubuk, E. D.; et al. Structure-property relationships from universal signatures of plasticity in disordered solids. *Science* **2017**, *358*, 1033−1037.

(15) Jang, D.; Greer, J. R. Transition from a strong-yet-brittle to a stronger-and-ductile state by size reduction of metallic glasses. *Nat. Mater.* **2010**, *9*, 215−219.

(16) Jang, D.; Gross, C. T.; Greer, J. R. Effects of size on the strength and deformation mechanism in Zr-based metallic glasses. *Int. J. Plast.* **2011**, *27*, 858−867.

(17) Greer, A. L.; Cheng, Y. Q.; Ma, E. Shear bands in metallic glasses. *Mater. Sci. Eng., R* **2013**, *74*, 71−132.

(18) Ding, B.; et al. Brittle versus ductile fracture mechanism transition in amorphous lithiated silicon: From intrinsic nanoscale cavitation to shear banding. *Nano Energy* **2015**, *18*, 89−96.

(19) Zhou, X.; Zhou, H.; Li, X.; Chen, C. Size effects on tensile and compressive strengths in metallic glass nanowires. *J. Mech. Phys. Solids* **2015**, *84*, 130−144.

(20) Schall, P.; Weitz, D. A.; Spaepen, F. Structural rearrangements that govern flow in colloidal glasses. *Science* **2007**, *318*, 1895−1899.

(21) Strickland, D. J.; Huang, Y.-R.; Lee, D.; Gianola, D. S. Robust scaling of strength and elastic constants and universal cooperativity in disordered colloidal micropillars. *Proc. Natl. Acad. Sci. U. S. A.* **2014**, *111*, 18167−18172.

(22) Richard, D.; et al. Predicting plasticity in disordered solids from structural indicators. *Phys. Rev. Mater.* **2020**, *4*, 113609.

(23) Argon, A. S. Plastic deformation in metallic glasses. *Acta Metall.* **1979**, *27*, 47−58.

(24) Scott, G. D. Packing of equal spheres. *Nature* **1960**, *188*, 908.

(25) Bi, D.; Zhang, J.; Chakraborty, B.; Behringer, R. P. Jamming by shear. *Nature* **2011**, *480*, 355−358.

(26) Singh, A.; Ness, C.; Seto, R.; de Pablo, J. J.; Jaeger, H. M. Shear thickening and jamming of dense suspensions: the "roll" of friction. *Phys. Rev. Lett.* **2020**, *124*, 248005.
(27) Mo, Y.; Turner, K. T.; Szlufarska, I. Friction laws at the nanoscale. *Nature* **2009**, *457*, 1116−1119.
(28) Mate, C. M.; Carpick, R. W. *Tribology on the Small Scale: A Modern Textbook on Friction, Lubrication, and Wear*; OUP Oxford, 2019.
(29) Lee, D.; Rubner, M. F.; Cohen, R. E. All-nanoparticle thin-film coatings. *Nano Lett.* **2006**, *6*, 2305−2312.
(30) Wu, Z.; Lee, D.; Rubner, M. F.; Cohen, R. E. Structural color in porous, superhydrophilic, and self-cleaning SiO_2/TiO_2 Bragg stacks. *Small* **2007**, *3*, 1445−1451.
(31) Park, K.; Seo, D.; Lee, J. Conductivity of silver paste prepared from nanoparticles. *Colloids Surf., A* **2008**, *313*, 351−354.
(32) Cook, K. T.; Tettey, K. E.; Bunch, R. M.; Lee, D.; Nolte, A. J. One-step index-tunable antireflection coatings from aggregated silica nanoparticles. *ACS Appl. Mater. Interfaces* **2012**, *4*, 6426−6431.
(33) Huang, Y.-R.; Park, J. T.; Prosser, J. H.; Kim, J. H.; Lee, D. Multifunctional all-TiO_2 Bragg stacks based on blocking layer-assisted spin coating. *J. Mater. Chem. C* **2014**, *2*, 3260−3269.
(34) Park, J. T.; Kim, J. H.; Lee, D. Excellent anti-fogging dye-sensitized solar cells based on superhydrophilic nanoparticle coatings. *Nanoscale* **2014**, *6*, 7362−7368.
(35) Tan, S.; Hashim, H.; Lee, C.; Taib, M. R.; Yan, J. Economical and environmental impact of waste-to-energy (WTE) alternatives for waste incineration, landfill and anaerobic digestion. *Energy Procedia* **2014**, *61*, 704−708.
(36) Soliveri, G.; et al. Microwave-assisted silver nanoparticle film formation for SERS applications. *J. Phys. Chem. C* **2016**, *120*, 1237−1244.
(37) Stein, P.; Moradabadi, A.; Diehm, M.; Xu, B.-X.; Albe, K. The influence of anisotropic surface stresses and bulk stresses on defect thermodynamics in $LiCoO_2$ nanoparticles. *Acta Mater.* **2018**, *159*, 225−240.
(38) Jiang, Y.; Hor, J. L.; Lee, D.; Turner, K. T. Toughening nanoparticle films via polymer infiltration and confinement. *ACS Appl. Mater. Interfaces* **2018**, *10*, 44011−44017.
(39) Trappe, V.; Prasad, V.; Cipelletti, L.; Segre, P. N.; Weitz, D. A. Jamming phase diagram for attractive particles. *Nature* **2001**, *411*, 772−775.
(40) Lois, G.; Blawzdziewicz, J.; O'Hern, C. S. Jamming transition and new percolation universality classes in Particulate Systems with Attraction. *Phys. Rev. Lett.* **2008**, *100*, 028001.
(41) Martin, C. L.; Bordia, R. K. Influence of adhesion and friction on the geometry of packings of spherical particles. *Phys. Rev. E* **2008**, *77*, 031307.
(42) Parteli, E. J.; et al. Attractive particle interaction forces and packing density of fine glass powders. *Sci. Rep.* **2015**, *4*, 6227.
(43) Liu, W.; Li, S.; Baule, A.; Makse, H. A. Adhesive loose packings of small dry particles. *Soft Matter* **2015**, *11*, 6492−6498.
(44) Ma, X.; Liu, J.; Zhang, Y.; Habdas, P.; Yodh, A. Excess entropy and long-time diffusion in colloidal fluids with short-range interparticle attraction. *J. Chem. Phys.* **2019**, *150*, 144907.
(45) Munjiza, A. A. *The Combined Finite-Discrete Element Method*; John Wiley & Sons, 2004.
(46) Sauer, R. A.; Li, S. A contact mechanics model for quasi-continua. *Int. J. Numer. Methods Eng.* **2007**, *71*, 931−962.
(47) Luding, S. Cohesive, frictional powders: contact models for tension. *Granular Matter* **2008**, *10*, 235−246.
(48) Li, S.; Marshall, J. S.; Liu, G.; Yao. Q. Adhesive particulate flow: the discrete-element method and its application in energy and environmental engineering. *Prog. Energy Combust. Sci.* **2011**, *37*, 633−668.
(49) Thornton, C.; Cummins, S. J.; Cleary, P. W. An investigation of the comparative behaviour of alternative contact force models during inelastic collisions. *Powder Technol.* **2013**, *233*, 30−46.
(50) Marshall, J. S.; Li, S. *Adhesive Particle Flow*; Cambridge University Press, 2014.
(51) Plimpton, S. Fast parallel algorithms for short-range molecular dynamics. *J. Comput. Phys.* **1995**, *117*, 1−19.
(52) Israelachvili, J. N. *Intermolecular and Surface Forces*; Elsevier Science, 2011.
(53) Shimizu, F.; Ogata, S.; Li, J. Theory of shear banding in metallic glasses and molecular dynamics calculations. *Mater. Trans.* **2007**, *48*, 2923−2927.
(54) Li, J. AtomEye: an efficient atomistic configuration viewer. *Modell. Simul. Mater. Sci. Eng.* **2003**, *11*, 173.
(55) Goldenberg, C.; Goldhirsch, I. Friction enhances elasticity in granular solids. *Nature* **2005**, *435*, 188.
(56) Oliver, W. C.; Pharr, G. M. An improved technique for determining hardness and elastic modulus using load and displacement sensing indentation experiments. *J. Mater. Res.* **1992**, *7*, 1564−1583.
(57) Rottler, J.; Schoenholz, S. S.; Liu, A. J. Predicting plasticity with soft vibrational modes: from dislocations to glasses. *Phys. Rev. E* **2014**, *89*, 042304.
(58) Patinet, S.; Vandembroucq, D.; Falk, M. L. Connecting local yield stresses with plastic activity in amorphous solids. *Phys. Rev. Lett.* **2016**, *117*, 045501.
(59) Reynolds, O. On the dilatancy of media composed of rigid particles in contact, with experimental illustrations. *Philos. Mag. Ser.* **1885**, *20*, 469−481.
(60) Sadati, M.; Taheri Qazvini, N.; Krishnan, R.; Park, C. Y.; Fredberg, J. J. Collective migration and cell jamming. *Differentiation* **2013**, *86*, 121−125.
(61) Zheng, W.; Liu, H.; Xu, N. Shear-induced solidification of athermal systems with weak attraction. *Phys. Rev. E* **2016**, *94*, 062608.
(62) Liu, A. J.; Nagel, S. R. Nonlinear dynamics: jamming is not just cool any more. *Nature* **1998**, *396*, 21−22.
(63) Das, B. M.; Sobhan, K. *Principles of Geotechnical Engineering*; Cengage Learning, 2013.
(64) Gao, Y. F.; Wang, L.; Bei, H.; Nieh, T. G. On the shear-band direction in metallic glasses. *Acta Mater.* **2011**, *59*, 4159−4167.
(65) Rudnicki, J. W.; Rice, J. R. Conditions for the localization of deformation in pressure-sensitive dilatant materials. *J. Mech. Phys. Solids* **1975**, *23*, 371−394.

https://doi.org/10.1021/acs.nanolett.1c01952
Nano Lett. XXXX, XXX, XXX−XXX

SUPPORTING INFORMATION

Friction and Adhesion Govern Yielding of Disordered Nanoparticle Packings: A Multiscale Adhesive Discrete Element Method Study

Xiaohui Liu[1,2,3,†], Joel A. Lefever[4,§,†], Daeyeon Lee[5], Jie Zhang[6,7], Robert W. Carpick[8,*], Ju Li[3,9,*]
[1] *Institute of Materials Modification and Modeling, School of Materials Science and Engineering, Shanghai Jiao Tong University, Shanghai 200240, China*
[2] *Materials Genome Initiative Center, Shanghai Jiao Tong University, Shanghai 200240, China*
[3] *Department of Nuclear Science and Engineering, Massachusetts Institute of Technology, Cambridge, Massachusetts 02139, USA*
[4] *Department of Materials Science and Engineering, University of Pennsylvania, Philadelphia, Pennsylvania 19104, USA*
[5] *Department of Chemical and Biomolecular Engineering, University of Pennsylvania, Philadelphia, Pennsylvania 19104, USA*
[6] *Institute of Natural Sciences, Shanghai Jiao Tong University, Shanghai 200240, China*
[7] *School of Physics and Astronomy, Shanghai Jiao Tong University, Shanghai 200240, China*
[8] *Department of Mechanical Engineering and Applied Mechanics, University of Pennsylvania, Philadelphia, Pennsylvania 19104, USA*
[9] *Department of Materials Science and Engineering, Massachusetts Institute of Technology, Cambridge, Massachusetts 02139, USA*
[§] *Current Affiliation: Asylum Research – an Oxford Instruments Company, Santa Barbara, California 93117, USA*
[†] *X. Liu and J. Lefever contributed equally*
[*] *To whom correspondence should be addressed: carpick@seas.upenn.edu (R. Carpick) or liju@mit.edu (J. Li)*

CONTENTS

I. MULTISCALE ADHESIVE DISCRETE ELEMENT METHOD

Traditional discrete element method (DEM) [1] has been extensively applied to investigate the properties of granular packings consisting of repulsive particles. DEM captures the interaction forces and torques on the particles during the course of collisions, and numerically solves Newton's equations of the translational and rotational motion for individual particles. Conventionally, the interparticle collision can be decomposed into normal contact, sliding, twisting, and rolling [2], as shown in Fig. S1. For normal contact, the seminal Hertz theory [3] is commonly employed to describe the normal elastic contact force in traditional DEM. However, when the particle size reduces, interparticle adhesion can become non-negligible. Since the 1970s, several analytical adhesive contact models such as the JKR [4], DMT [5], and MD [6] theory have been proposed, applicable to various combinations of the characteristic length scale of contact, the elastic stiffness, and the range of the adhesive forces, as summarized in the Johnson-Greenwood adhesion map [7]. Nevertheless, all these models are based on linear elasticity and restricted to infinitesimal deformation, and can only handle the mechanical response within the contact regime. In our nanoparticle packing system, the particles beneath the atomic force microscopy (AFM) probe could undergo large deformation. Moreover, as we will see below, the adhesive force even prior to contact are non-negligible between two particles, because the van der Waals interaction turns to be long-ranged when the particle size is at the nano scale. This substantially influences the packing configuration as well as the macroscopic structural properties.

In the present study, following previous work [8], we describe the normal elastic contact between deformable particles via a multiscale adhesive contact model, incorporating the interaction between molecules or atoms within particles in neighbor. This model is implemented within a nonlinear finite element (FE) formulation, which is able to simulate a full-range interparticle adhesive normal contact process involving large deformation. We propose a robust methodology in a target of effectively extracting the normal elastic contact force between particles with various effective radii based on very limited FE simulation results. By incorporating the conventional models [2, 9–11] for the three other modes of particle interactions due to friction shown in Fig. S1, we establish a multiscale adhesive discrete element method (MADEM), implemented in the LAMMPS code [12]. The theories of the particle interactions in the MADEM will be described in more detail below, with special emphasis on the normal contact. Only spherical particles will be considered.

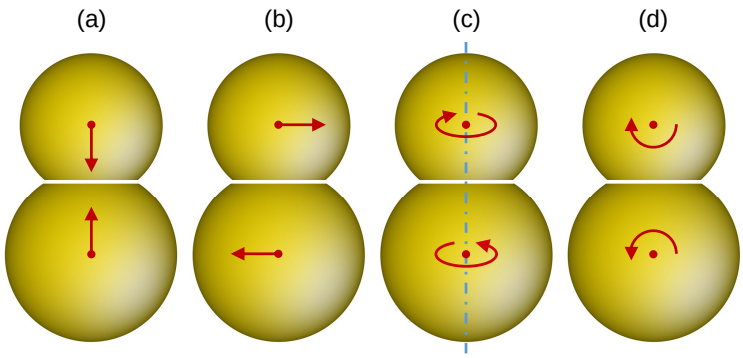

FIG. S1. Modes of particle interaction: (a) normal contact, (b) sliding, (c) twisting, and (d) rolling [2].

- **Normal contact**

Normal contact induces opposite forces on two particles in collision along their normal direction. The Kelvin spring-dashpot model [13] has been widely used to compute the total normal contact force $\mathbf{F}_n$, which is the sum of the normal elastic force $\mathbf{F}_{ne}$ and the normal dissipative force $\mathbf{F}_{nd}$. To model the normal contact force, the contact between two elastic spherical particles with radii R_α, elastic moduli E_α and Poisson's ratios ν_α ($\alpha = i, j$) (Fig. S2) is usually simplified into that between an elastic sphere and a semi-infinite rigid plane, with the effective radius R, mass M, elastic modulus E and shear modulus G defined by

$$\frac{1}{R} \equiv \frac{1}{R_i} + \frac{1}{R_j}, \frac{1}{M} \equiv \frac{1}{M_i} + \frac{1}{M_j}, \frac{1}{E} \equiv \frac{1-\nu_i^2}{E_i} + \frac{1-\nu_j^2}{E_j}, \frac{1}{G} \equiv \frac{2-\nu_i}{G_i} + \frac{2-\nu_j}{G_j}. \tag{1}$$

The adhesion is attributed to the interaction between the molecules within the sphere and the rigid plane. For our disordered nanoparticle packings (DNPs), it could involve the van der Waals interaction, covalent bonding, hydrogen bonding, etc. For simplicity, first we only consider the van der Waals interaction, and describe it by the 12/6

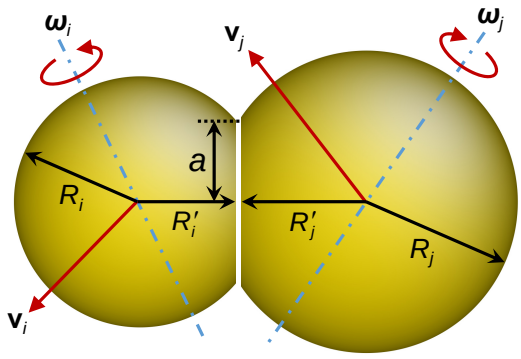

FIG. S2. Schematics of contact between two spherical particles. R_α is the radius of particle α ($\alpha = i, j$), R'_α is the corrected radius, $\mathbf{v}_\alpha$ is the translational velocity, $\boldsymbol{\omega}_\alpha$ is the rotational angular velocity, and a is the contact radius.

Lennard-Jones potential

$$\phi(r) = 4\epsilon \left[\left(\frac{\sigma}{r}\right)^{12} - \left(\frac{\sigma}{r}\right)^{6} \right], \tag{2}$$

in which ϵ is the depth of the potential well, σ is the finite distance at which the potential is zero, and r is the intermolecular distance. By integrating over the entire volume bounded by the semi-infinite plane, the adhesive body force in the sphere per unit volume at a distance D away from the surface of the rigid plane is then given by

$$B(D) = \frac{A_{ij}}{\pi\sigma^4} \left[\frac{1}{5} \left(\frac{\sigma}{D}\right)^{10} - \frac{1}{2} \left(\frac{\sigma}{D}\right)^{4} \right]. \tag{3}$$

Here A_{ij} is the Hamaker constant [14], expressed as

$$A_{ij} = 4\pi\sigma^6 \rho_i \rho_j \epsilon, \tag{4}$$

in which ρ_i and ρ_j are the molecular number density of the sphere and the rigid plane, respectively. It can be further approximated to be

$$A_{ij} = \sqrt{A_{ii} A_{jj}}, \tag{5}$$

where A_{ii} and A_{jj} are the Hamaker constants for the individual molecular species of the sphere and the rigid plane, respectively, which can be measured experimentally or determined computationally. The parameter σ can be connected to the equilibrium separation z_0 between two rigid planes with the same intermolecular interaction given in Eq. (2) by

$$z_0 = \left(\frac{2}{15}\right)^{\frac{1}{6}} \sigma, \tag{6}$$

in which the value of 0.165 nm for z_0 fits well with many materials [2]. This further allows us to calculate the work of adhesion w_0 as [6]

$$w_0 = \frac{A_{ij}}{16\pi z_0^2}, \tag{7}$$

which is the work required to separate the two rigid planes from the equilibrium position to infinity.

We employ the compressible Neo-Hookean hyperelasticity model [15] to describe the non-linear elastic deformation of the sphere, whose strain energy density W takes the form

$$W = \frac{\mu}{2}(I_1 - 3) - \mu \ln J + \frac{\lambda}{2} (\ln J)^2, \tag{8}$$

where μ and λ are the Lamé constants of the material, J is the determinant of the deformation gradient tensor $\mathbf{F}$, and I_1 is the trace of $\mathbf{F}^T\mathbf{F}$. The Cauchy stress tensor $\boldsymbol{\sigma}$ and the tangent elasticity tensor $\mathbf{C}$ are then given by

$$\boldsymbol{\sigma} = \frac{\lambda}{J} (\ln J)\, \mathbf{I} + \frac{\mu}{J} \left(\mathbf{F}^T\mathbf{F} - \mathbf{I}\right), \tag{9}$$

$$\mathbf{C} = \frac{\lambda}{J} \mathbf{I} \otimes \mathbf{I} + \frac{2}{J} (\mu - \lambda)\, \mathbf{II}, \tag{10}$$

TABLE S1. Parameters used in the FE simulations of the particle-particle (P-P), particle-indenter (P-I) and particle-substrate (P-S) contact. The subscript i denotes silica particle and j denotes silica particle, diamond indenter or silicon substrate interacted with particle i. The Hamaker constant A of the particle is chosen for that of the α-alumina coating.

	R_i (nm)	E_i (GPa)	ν_i	A_i (10^{-20} J)	R_j (nm)	E_j (GPa)	ν_j	A_j (10^{-20} J)	R (nm)	E (GPa)	w_0 (mJ/m^2)
P-P	7.6				7.6	70	0.17	15	3.8	36.04	109.62
	12.4				12.4				6.2		
P-I	7.6	70[a]	0.17[a]	15[b]	16.7	1143[c]	0.069[c]	29.6[b]	5.22	67.83	153.98
	12.4								7.12		
P-S	7.6				∞	150[d]	0.17[d]	20[b]	7.6	49.15	126.56
	12.4								12.4		

[a]Ref. [16]; [b]Ref. [14]; [c]Ref. [17]; [d]Ref. [18]

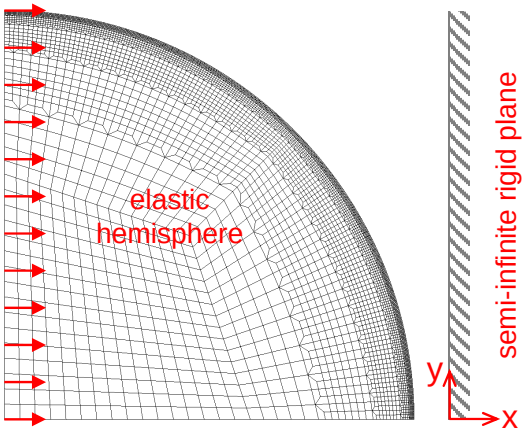

FIG. S3. Mesh and boundary conditions for the FE simulation of the contact between an elastic hemisphere and a semi-infinite rigid plane. The mesh of the hemisphere consists of linear four-node axisymmetric elements with respect to the x axis. The arrows indicate a prescribed displacement boundary condition applied on the central plane of the hemisphere.

where **I** and **II** are the second order and fourth order identity tensors, respectively.

We then carry out FE simulations of the full-range contact between the sphere and the rigid plane based on the adhesive and mechanical constitutive models above, implemented in a commercial FE package, MSC.Marc [19]. We take into account the interactions between particle-particle (P-P), particle-indenter (P-I), and particle-substrate (P-S). For each case, two different sphere radii are considered to cover the range of the particle size distribution of 20.0±4.8 nm diameter in prior experiments [20]. The indenter radius is set to 16.7 nm to match the experimentally measured tip size [20]. Table S1 lists the radii of the sphere and the effective moduli used in the FE simulations. Fig. S3 shows the FE mesh of the hemisphere we use, which is axisymmetric with respect to the x axis. The mesh is specially refined from the central plane of the hemisphere to the surface since the surface area bears larger strain and adhesive force, and we have found that the value of F_{ne} is converged with this mesh refinement. A prescribed displacement is applied on the central plane of the hemisphere to drive it to approach the rigid plane. The indentation depth δ is defined as $R-h$, where h is the distance from the central plane of the hemisphere to the rigid plane. The range of δ covered in the simulation is $[-1$ nm, $0.5R]$ with a change in δ of 0.1 nm in each increment. The force corresponding to a depth beyond this range is obtained by linear interpolation based on the F_{ne}-δ data of the last two points on the bound. This indicates that the interparticle potential energy has a second-order polynomial cutoff of $\delta_{\rm cut}$ larger than -1 nm for two neighboring particles. In MADEM, at each time step, we calculate δ for each pair of neighboring particles. An interparticle bond will form (break) if δ between two particles is greater (less) than the respective $\delta_{\rm cut}$.

Fig. S4 presents a snapshot of the distribution of the normal stress in the normal direction within the hemisphere in contact with the rigid plane, showing the tensile stress state on the contact edge due to the adhesion. The normal elastic force is extracted by summation of the reaction force of all the nodes on the central plane of the hemisphere. Fig. S5 shows the F_{ne}-δ curves of the P-P, P-I and P-S contact by the FE simulations. To investigate the effect of the

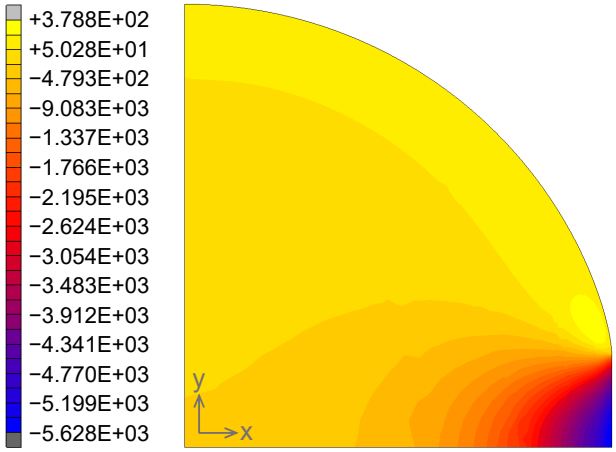

FIG. S4. Distribution of the normal stress σ_{xx} (in MPa) for particle-particle contact with $w = w_0^{\text{P-P}}$ and $R = 5$ nm at $\delta = 0$ nm.

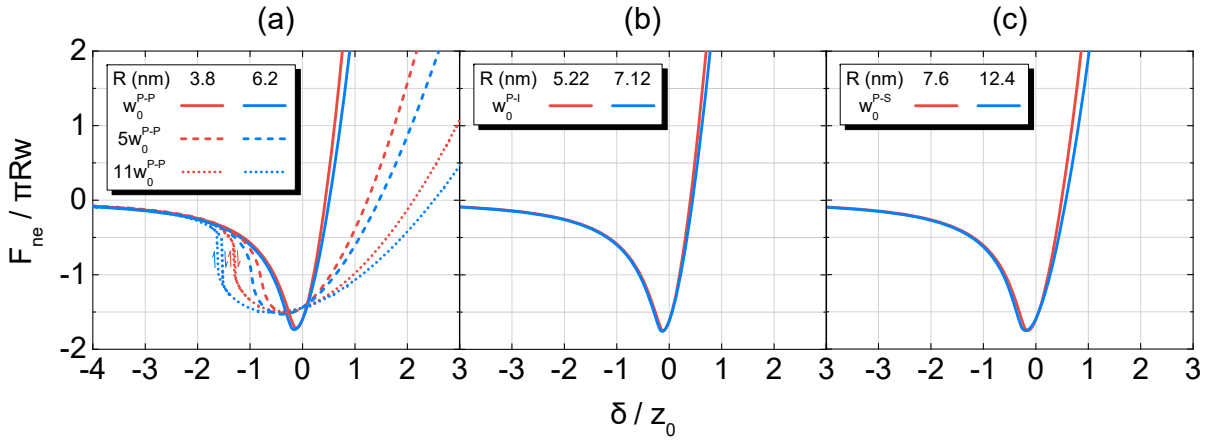

FIG. S5. F_{ne}-δ curves with various R and w for (a) particle-particle (b) particle-indenter and (c) particle-substrate interactions. The arrows in (a) indicate the difference in the loading and unloading curves due to jump on and jump off in the case of strong adhesion.

adhesion strength on the properties of the nanoparticle packing, various work of adhesion values w from w_0 to $11w_0$ for the P-P interaction have been considered by simply boosting the value of ϵ in Eq. (2). For the cases of high work of adhesion, the well-known jump-on and jump-off phenomena [2] are observed in the loading and unloading processes, respectively. For simplicity, we only use the loading curves as the input in MADEM simulations, since there is no significant difference between the loading and unloading curves.

Since our nanoparticle packings are polydisperse, it is unrealistic to obtain all the F_{ne}-δ data for all possible effective radii by FE simulation. Here we develop a fitting methodology based on an analytical adhesive contact model, which is able to effectively produce the F_{ne}-δ curve for an arbitrary effective radius using those shown in Fig. S5. We choose the DMT model [5] for the fitting because of its simple form, though our calculation of the Maugis parameter [6] indicates that the particle interaction is within the MD (intermediate) regime on the Johnson-Greenwood adhesion map [7]. The DMT model gives

$$F_{ne} = \frac{4}{3} E \delta^{3/2} \sqrt{R} - 2\pi R w, \tag{11}$$

which can be rewritten as

$$\frac{F_{ne}}{\sqrt{R}} = \frac{4}{3} E \delta^{3/2} - 2\pi \sqrt{R} w. \tag{12}$$

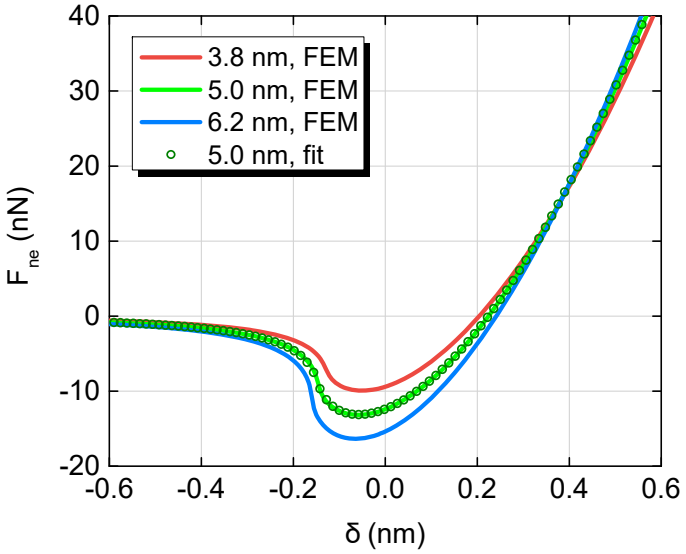

FIG. S6. Comparison of the F_{ne}-δ curve for particle-particle contact with $w = 5w_0^{\text{P-P}}$ and $R = 5.0$ nm by the FE simulation with that fitted by Eq. (13) using the $R_1 = 3.8$ nm and $R_2 = 6.2$ nm curves.

The above linear relation between $F_{ne}/\sqrt{R}$ and $\sqrt{R}$ allows us to fit F_{ne} for a given R by

$$\frac{F_{ne}}{\sqrt{R}} = \frac{F_{ne1}}{\sqrt{R_1}} + \left(\frac{F_{ne2}}{\sqrt{R_2}} - \frac{F_{ne1}}{\sqrt{R_1}}\right)\frac{\sqrt{R}-\sqrt{R_1}}{\sqrt{R_2}-\sqrt{R_1}}, \tag{13}$$

in which F_{ne1} and F_{ne2} are the normal elastic forces for R_1 and R_2, respectively. As an example, Fig. S6 compares the fitted F_{ne} curve for a P-P interaction of $R = 5.0$ nm with that by the FE simulation. They agree well with each other even in the out-of-contact stage, which validates the effectiveness of our fitting scheme. This methodology is implemented in our MADEM code for the on-the-fly fitting.

The normal dissipative force F_{nd} between two particles, according to the dashpot model [10, 13], is given by

$$\mathbf{F}_{nd} = \gamma_n\sqrt{Mk_n}\,(\mathbf{v}_{re}\cdot\mathbf{n})\,\mathbf{n}. \tag{14}$$

Here γ_n is the normal viscous damping coefficient, k_n is the normal spring stiffness given by $2Ea$, $\mathbf{v}_{re}$ is the relative velocity at the contact point, and $\mathbf{n}$ is the unit vector in the normal direction between the centroids of the two particles. We follow Maugis' scheme [6] to extract the contact radius a from the FE simulation in the case of adhesion. The relative velocity $\mathbf{v}_{re}$ is the consequence of both the translational and rotational motion of the two particles, such that

$$\mathbf{v}_{re} = \left(\mathbf{v}_j - R'_j\boldsymbol{\omega}_j\times\mathbf{n}\right) - \left(\mathbf{v}_i - R'_i\boldsymbol{\omega}_i\times\mathbf{n}\right). \tag{15}$$

Here, as shown in Fig. S2, $\mathbf{v}_\alpha$ and $\boldsymbol{\omega}_\alpha$ are the translational velocity and rotational angular velocity of particle α, respectively, and R'_α is the corrected radius, which can be estimated using the Hertz contact theory by

$$R'_\alpha = R_\alpha - \frac{1-\nu_\alpha^2}{E_\alpha}E\delta. \tag{16}$$

The total normal contact forces on particle i and j are then given by

$$\mathbf{F}_{ni} = -\mathbf{F}_{nj} = F_{ne}\mathbf{n} + \mathbf{F}_{nd} = \left(F_{ne} + \gamma_n\sqrt{Mk_n}\mathbf{v}_{re}\cdot\mathbf{n}\right)\mathbf{n}. \tag{17}$$

- **Sliding**

Sliding motion induces both the frictional force and torque on two particles in contact. Here we employ the well-known linear spring-dashpot model [10, 13]. The frictional force $\mathbf{F}_s$ due to sliding is given by

$$\mathbf{F}_{se}^n = \begin{cases} \mathbf{F}_{se}^{n-1} + k_s^n\Delta\mathbf{u}_s^n, & \text{if } \Delta a \geq 0 \\ \mathbf{F}_{se}^{n-1}\frac{k_s^n}{k_s^{n-1}} + k_s^n\Delta\mathbf{u}_s^n, & \text{if } \Delta a < 0, \end{cases} \tag{18}$$

$$\mathbf{F}_s = \mathbf{F}_{se}^n + \gamma_s\sqrt{Mk_s}\mathbf{v}_s. \tag{19}$$

Here Δa is the change of the contact radius, the sign of whose value signifies the normal loading or unloading, k_s is the tangential stiffness given by $8Ga$, γ_s is the tangential viscous damping coefficient, $\Delta\mathbf{u}_s^n$ is the relative tangential displacement in the current time step given by $\mathbf{v}_s\Delta t$, where Δt is the timestep, and $\mathbf{v}_s$ is the relative tangential velocity at the contact point, given by

$$\mathbf{v}_s = \mathbf{v}_{re} - (\mathbf{v}_{re}\cdot\mathbf{n})\,\mathbf{n}. \tag{20}$$

The sliding frictional force needs to be further checked to determine whether it satisfies the Coulomb-like yield condition in the case of adhesion. Here we truncate the magnitude of $\mathbf{F}_s$ following Refs. [21, 22] by

$$|\mathbf{F}_s| \le \mu_s\,|F_n + 2F_p|\,, \tag{21}$$

in which μ_s is the dynamic friction coefficient for sliding, $F_n = \mathbf{F}_n\cdot\mathbf{n}$, and F_p is the pull-off force, the negative of the minimum force on the F_{ne}-δ curve.

The sliding force exerts torques on both particles in contact, which for particle α is

$$\mathbf{T}_{s\alpha} = -R'_\alpha\mathbf{n}\times\mathbf{F}_s. \tag{22}$$

- **Twisting**

The twisting resistance imposes torques on two particles in contact along their normal direction. Following the same logic in the sliding model, we calculate the twisting resistance force $\mathbf{F}_t$ as

$$\mathbf{F}_{te}^n = \begin{cases} \mathbf{F}_{te}^{n-1} + k_t^n\Delta\mathbf{u}_t^n, & \text{if } \Delta a \ge 0 \\ \mathbf{F}_{te}^{n-1}\frac{k_t^n}{k_t^{n-1}} + k_t^n\Delta\mathbf{u}_t^n, & \text{if } \Delta a < 0, \end{cases} \tag{23}$$

$$\mathbf{F}_t = \mathbf{F}_{te}^n + \gamma_t\sqrt{Mk_t}\mathbf{v}_t. \tag{24}$$

Here k_t is the twisting stiffness, γ_t is the twisting viscous damping coefficient, $\Delta\mathbf{u}_t^n$ is the relative twisting displacement in the current time step given by $\mathbf{v}_t\Delta t$, where $\mathbf{v}_t$ is the relative twisting velocity at the contact edge, given by

$$\mathbf{v}_t = a\,(\boldsymbol{\omega}_i\cdot\mathbf{n} - \boldsymbol{\omega}_j\cdot\mathbf{n})\,\mathbf{n}. \tag{25}$$

The twisting resistance force activates torques with opposite directions on the two particles i and j, which are

$$\mathbf{T}_{ti} = -\mathbf{T}_{tj} = a\mathbf{F}_t. \tag{26}$$

Similar to the case of $\mathbf{F}_s$, the magnitude of $\mathbf{T}_t$ needs to be truncated as required to satisfy the elastic yield condition for twisting, as given by [23]

$$|\mathbf{T}_t| \le \frac{3\pi}{16}a\mu_s\,|F_n + 2F_p|\,. \tag{27}$$

This condition is equivalent to

$$|\mathbf{F}_t| \le \mu_t\,|F_n + 2F_p|\,, \tag{28}$$

in which μ_t is the twisting friction coefficient with $\mu_t/\mu_s = 3\pi/16$.

- **Rolling**

We follow the same methodology as those used for modeling the sliding and twisting above to obtain the torques induced by the rolling resistance. Similarly, we introduce the rolling resistance force $\mathbf{F}_r$ as

$$\mathbf{F}_{re}^n = \begin{cases} \mathbf{F}_{re}^{n-1} + k_r^n\Delta\mathbf{u}_r^n, & \text{if } \Delta a \ge 0 \\ \mathbf{F}_{re}^{n-1}\frac{k_r^n}{k_r^{n-1}} + k_r^n\Delta\mathbf{u}_r^n, & \text{if } \Delta a < 0, \end{cases} \tag{29}$$

$$\mathbf{F}_r = \mathbf{F}_{re}^n + \gamma_r\sqrt{Mk_r}\mathbf{v}_r. \tag{30}$$

Here k_r is the rolling stiffness, γ_r is the rolling viscous damping coefficient, $\Delta\mathbf{u}_r^n$ is the relative rolling displacement in the current time step given by $\mathbf{v}_r\Delta t$, where $\mathbf{v}_r$ is the relative rolling velocity, defined as [9]

$$\mathbf{v}_r = -R'\,(\mathbf{n}\times\boldsymbol{\omega}_i - \mathbf{n}\times\boldsymbol{\omega}_j)\,. \tag{31}$$

Here R' is the effective corrected radius with $1/R' \equiv 1/R'_i + 1/R'_j$. The magnitude of $\mathbf{F}_r$, according to the elastic yield criterion, is bounded by

$$|\mathbf{F}_r| \leq \mu_r \left| F_n + 2F_p \right|, \tag{32}$$

where μ_r is the rolling friction coefficient. The torques on the contacted particles i and j due to rolling are then given by

$$\mathbf{T}_{ri} = -\mathbf{T}_{rj} = a\mathbf{n} \times \mathbf{F}_r. \tag{33}$$

Along with Table 1 in the main text, Table S2 lists the additional parameters introduced in the above models of normal contact, sliding, twisting and rolling for the MADEM simulations. We find that the damping of sliding, twisting and rolling plays a negligible role in the mechanical response by varying the damping coefficients over the range of $0-1$ ns^{-1} tested. For simplicity, we set these coefficients to be zero.

TABLE S2. Additional parameters used in the MADEM simulations.

Parameter	Value	Reference
k_t/k_s	0.5	[9]
k_r/k_t	1.0	[9]
μ_t/μ_s	$3\pi/16$	[2]
μ_r/μ_t	1.0	[9]
γ_n	0.4 ns^{-1}	Chosen to avoid overdamping
γ_s	0.0 ns^{-1}	Load curve is insensitive to γ_s
γ_t	0.0 ns^{-1}	Load curve is insensitive to γ_t
γ_r	0.0 ns^{-1}	Load curve is insensitive to γ_r

II. ERROR ANALYSIS OF THE ADHESIVE FORCE BETWEEN A COATED SPHERE AND A SEMI-INFINITE PLANE

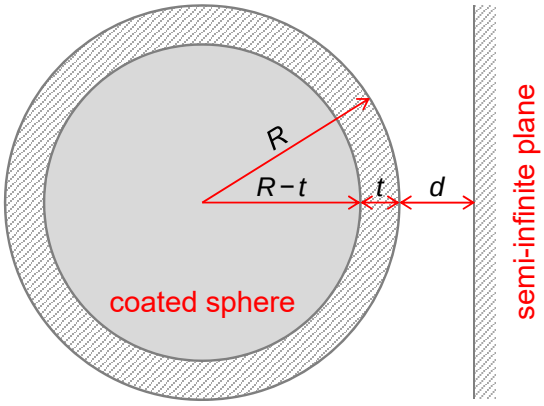

FIG. S7. Schematic of the interaction between a coated sphere and a semi-infinite plane. R is the radius of the coated sphere, t is the thickness of the coating, and d is the gap between the sphere and the plane.

As mentioned in the main text and Sec. I above, we approximately obtain the default work of adhesion between the alumina-coated silica particles based on the Hamaker constant of α-alumina, considering that the interaction between interparticle molecules decays rapidly with increasing separation distance. However, this inevitably introduces an error in calculating the adhesive force since the Hamaker constant of silica (in the particle core) is different from that of alumina (in the particle coating). In this section, based on the analytical Derjaguin's approximation [24], we give an error analysis of the adhesive force between a coated sphere and a semi-infinite plane using the same Hamaker constant, benchmarked by that using different Hamaker constants.

According to the Derjaguin's approximation, the adhesive force F between a sphere with a radius R and a semi-infinite plane due to the van der Waals attraction is given by

$$F = -\frac{AR}{6d^2}, \tag{34}$$

where A is the Hamaker constant of the molecules within the sphere and the plane, and d is the gap between the sphere and the plane. If the molecular species within the sphere is different from that within the plane, whose Hamaker constants are A_s and A_p, respectively, the adhesive force is approximated to be

$$F = -\sqrt{A_s A_p}\frac{R}{6d^2}. \tag{35}$$

Now consider the interaction between a sphere with a coating thickness t and a semi-infinite plane, as shown in Fig. S7. Then the adhesive force F_0 is the sum of those of the core/plane attraction and the coating/plane attraction, which is

$$F_0 = -\sqrt{A_{\text{in}} A_p}\frac{R-t}{6(d+t)^2} - \sqrt{A_{\text{out}} A_p}\left[\frac{R}{6d^2} - \frac{R-t}{6(d+t)^2}\right]. \tag{36}$$

Here A_{in} and A_{out} are the Hamaker constants of the molecules in the core and in the coating of the sphere, respectively, and the Hamaker constant of the molecules within the plane is assumed to be a constant A_p. For simplicity, the effect of the coating (as a media) on the core/plane interaction is neglected. On the other hand, if we ignore the difference between A_{in} and A_{out}, the adhesive force can be simplified to

$$F_1 = -A_{\text{in}}\frac{R}{6d^2}, \tag{37}$$

or

$$F_2 = -A_{\text{out}}\frac{R}{6d^2}, \tag{38}$$

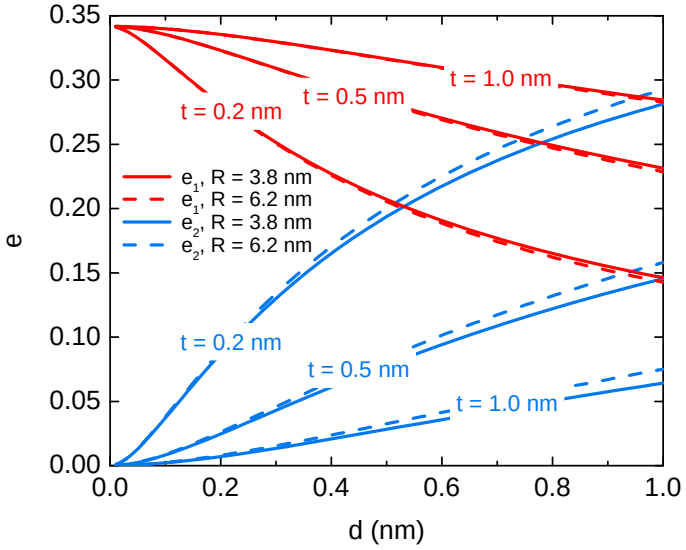

FIG. S8. e-d curves for various combinations of R and t based on Eqs. (39) and (40).

if both the Hamaker constants of the molecules within the sphere and the plane are chosen to be A_{in} and A_{out}, respectively. The errors in the adhesive forces by Eqs. (37) and (38) relative to that by Eq. (36) are then given by

$$e_1 \equiv \left|\frac{F_1 - F_0}{F_0}\right| = \frac{\left|1 - \sqrt{\frac{A_{\text{out}}}{A_{\text{in}}}}\right|}{\left[\left(1 + \frac{t}{d}\right)^2 - \left(1 - \frac{t}{R}\right)\right]^{-1} + \sqrt{\frac{A_{\text{out}}}{A_{\text{in}}}}}, \tag{39}$$

and

$$e_2 \equiv \left|\frac{F_2 - F_0}{F_0}\right| = \frac{\left|1 - \sqrt{\frac{A_{\text{in}}}{A_{\text{out}}}}\right|}{\left[\left(1 + \frac{t}{d}\right)^2 \left(1 - \frac{t}{R}\right)^{-1} - 1\right] + \left(1 - \frac{t}{R}\right)^{-1} \sqrt{\frac{A_{\text{in}}}{A_{\text{out}}}}}, \tag{40}$$

respectively.

Although we employ the MADEM approach rather than the Derjaguin's analytical formula to obtain the adhesive force considering that the particle undergoes deformation in contact with the rigid plane, Eqs. (39) and (40) should be good approximation to the error for the case of a deformed sphere, and d should be comparable to the indentation depth δ. In our DNPs, the range of R for P-P is [3.8 nm, 6.2 nm], and t is estimated to be less than 1 nm. Thus we can plot the e_1-d and e_2-d curves for various combinations of R and t, as shown in Fig. S8, with A_{in} and A_{out} chosen to be $A_{\text{silica}} = 6.5 \times 10^{-20}$ J and $A_{\alpha\text{-alumina}} = 15.0 \times 10^{-20}$ J, respectively [14]. It can be seen that e is sensitive to t but not to R as far as the ranges of the variables concerned, and e_1 (e_2) decreases (increases) with increasing d. In general, we conclude that $A_{\alpha\text{-alumina}}$ is a better choice than A_{silica} for calculating the work of adhesion for our DNPs, since within a cutoff d of 1 nm (beyond which the adhesive force approaches 0), e_2 is generally smaller than e_1, except for the case of very small t, in which (such as $t = 0.2$ nm) e_2 exceeds e_1 when d is greater than about 0.52 nm. Note, however, that for such a large d or δ, the adhesive force is already weak, as shown in Fig. S6, hence the apparent large e_2 will not yield significant deviation of absolute adhesive force. Even more noteworthy is that, as shown in Table 1 in the main text, we vary the work of adhesion by far more than e_2 shown here, meaning that the error in calculating the adhesive force by our approach makes little difference in evaluating the effects of the adhesion on the mechanical response of our DNPs.

III. PROTOCOLS FOR PREPARING NANOPARTICLE PACKINGS FOR INDENTATION SIMULATIONS AND PACKING FRACTION CALCULATION

Preparing packings for indentation simulations involves particle generation and equilibration. First, 4000 particles are generated sequentially with random diameters uniformly distributed within 20.0±4.8 nm, and with random positions in a box with an initial size $l_x \times l_y \times l_z$ of 200×200×200 nm^3. The box has periodic boundary conditions in the x and y directions, a silicon substrate on the bottom, and a near-rigid plate on the top. The interactions between the particles and the silicon substrate are based on the curves in Fig. S5c. The rigid top plate precisely controls the film thickness to be 200 nm. Second, under the condition of each work of adhesion value while without any friction, the box is gradually enlarged along the x and y directions simultaneously by minimization of the potential energy until the average of the pressures p_{xx} and p_{yy} is less than 1 MPa. Then l_x and l_y of the box are adjusted alternatively until both p_{xx} and p_{yy} are less than 10^{-10} MPa. This process is able to guarantee no significant difference between the final l_x and l_y values while maintaining their independence in the final stage of fine adjustment since p_{xx} and p_{yy} are essentially coupled with each other. Finally, the top plate is removed and the particles are relaxed again while keeping l_x and l_y fixed. The particle rearrangements during this step are minimal since p_{xx} and p_{yy} before this step are already small and the plate exerts little pressure on the surface particles on the top.

To directly compare load curves in studying the effect of friction on the mechanical response (Figs. 5a and 5c in the main text), we use the same initial equilibrium configuration and only change the friction coefficient in each individual simulation. By contrast, for studying the effect of work of adhesion (Figs. 5b and 5d in the main text), first we prepare a packing with work of adhesion value w_0 according to the above protocol. Then, starting from this initial configuration, we follow the same equilibration scheme above to obtain equilibrium packings with other work of adhesion values. By inspecting the changes in particle positions, we find that stronger adhesion results in a small amount of compression without any significant particle rearrangements. This guarantees certain similarities in the topology between the packings with various work of adhesion values, leading to comparability between the mechanical response of each packing.

The protocol for preparing the samples for the packing fraction calculation is different from that for indentation simulations, since the free surface has to be ruled out. Here, we employ a box with periodic boundary conditions in all the x, y and z directions. The initial box size is the same as that for indentation simulations above and the number of particles generated is doubled in order to reduce the uncertainty in calculating the packing fraction. The equilibration scheme is quite similar to that for indentation simulations, with the only difference in being that an additional pressure p_{zz} needs to be controlled. For each work of adhesion value, we use five different initial configurations to get the average packing fraction as well as the standard error.

IV. EFFECT OF THE WORK OF ADHESION ON PACKING FRACTION

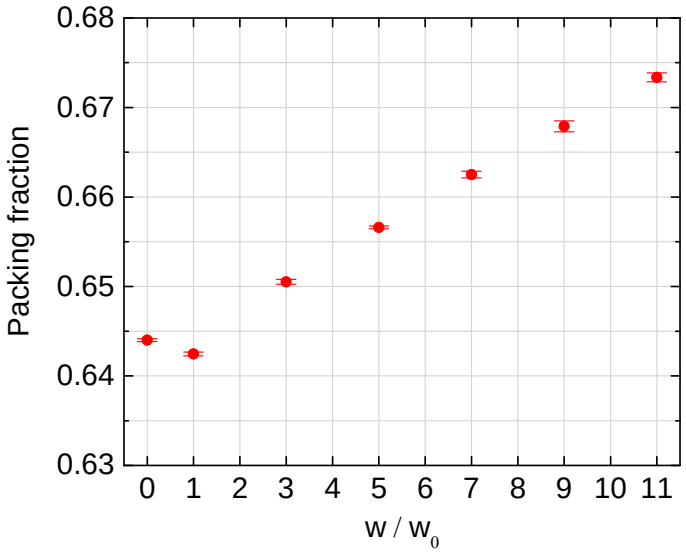

FIG. S9. The dependence of packing fraction on the work of adhesion for our DNPs without introducing friction. The error bars reflect the standard deviation of the packing fractions from five simulated packings, each with a different initial configuration. Friction is absent in preparing these packings.

The effect of the work of adhesion on the packing fraction of our DNPs is shown in Fig. S9 above. For the pure repulsive case ($w = 0$), the interparticle potential is obtained based on conventional contact mechanics FE simulations without introducing intermolecular interactions, and geometric contact is thus equivalent to physical contact [6]. In this case, as our packings are polydisperse, the close packing limit is above the commonly quoted value of 64% for random close-packed monodisperse spheres [25, 26]. The packing fraction decreases slightly in the presence of weak adhesion. This is because we use the van der Waals attraction and the Born repulsion to model the intermolecular force between two particles with adhesion (see Eq. (2)), which inevitably yields a geometric gap between the two particles even if they physically contact with each other, i.e., geometric contact can never been achieved [6]. This gap, which is absent in the interfaces between non-adhesive particles, has a non-negligible effect on the packing fraction when the size of the adhesive particles goes down to nanoscale. A further increase of the adhesion force enhances the packing fraction, signifying that the packing becomes denser with stronger adhesion.

It has been previously reported that increased adhesion can reduce the packing fraction of particles [27, 28]. This apparent contradiction can be explained by the fact that we use a loosening scheme from an initially densified state to equilibrate the packing (See the protocol given in Sec. III). This is opposite to the densification scheme [27] and also different from the deposition scheme [28], which can produce more clusters in the packing when particles bridge each other under stronger adhesion. On the other hand, loosening from an initially densified packing inhibits formation of clusters as well as topological pores, and adhesion shortens the average interparticle distance so as to densify the packing. These results demonstrate that the packing fraction as well as its tendency with the change of work of adhesion is quite protocol-dependent.

V. EFFECT OF THE INDENTER SIZE ON MECHANICAL RESPONSE

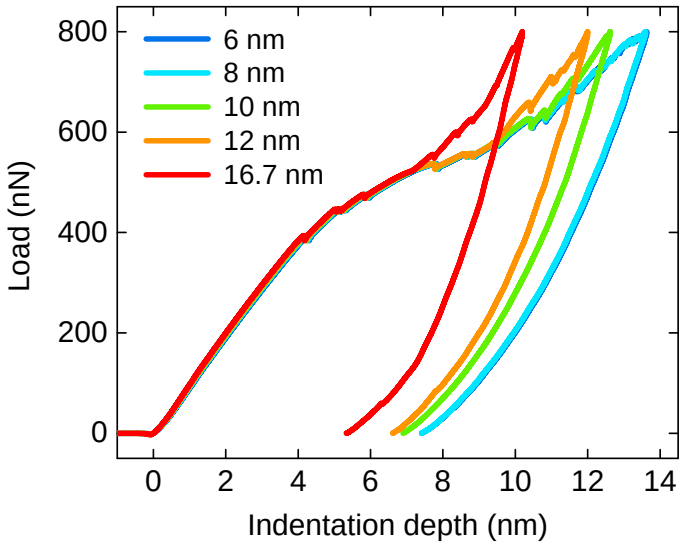

FIG. S10. Simulated indentation load curves at the same indent location of a DNP with various indenter radii (indicated in the legend). All the simulations have the same initial packing configuration, $\mu_s = 0.3$, $w = 7w_0$, and the maximum load of 800 nN. For comparison, the red curve has the experimentally-measured tip radius of 16.7 nm [20].

The effect of the indenter size on the mechanical response of a DNP under indentation is shown in Fig. S10. At shallow indentation depths (below approximately 4 nm), the indentation load L is insensitive to the change of the indenter radius r, in contrast with the relationship of $L \propto r^{1/2}$ in Hertz contact theory [3]. This can be explained by the fact that the contact stiffness between the diamond indenter and an individual particle is much higher than the local stiffness of the packing. If two springs with quite different stiffness are connected in series, the mechanical response is dominated by the more compliant one. Therefore, the load curves for shallow indentation depths in Fig. S10 largely reflect the local properties of the packings, and are barely affected by the contact stiffness (and thus the indenter size) between the indenter and the contacting particle. In the present simulations, the indenter is always positioned directly over a surface particle at the beginning of indentation, so the indenter does not make contact with multiple particles until later in the indentation cycle, if at all. With increasing the indentation depth, however, the load curves show that the indenter has a significant size effect in case of large r. This is because a larger indenter has more opportunity to contact more particles on the top surface in deep indents, which favors hardening. On the other hand, for an indenter which is small enough to contact only one particle during indentation, such as the cases of $r = 6$ nm and 8 nm, the size effect is remarkably diminished just like that in shallow indents. In order to prevent the indenter from making contact with multiple particles, thus affecting the mechanical response of DNPs, the default indenter radius used in simulation is set to 8 nm, only about one-half of the experimentally-measured tip radius (16.7 nm) [20].

VI. EFFECT OF THE INDENTATION VELOCITY ON MECHANICAL RESPONSE

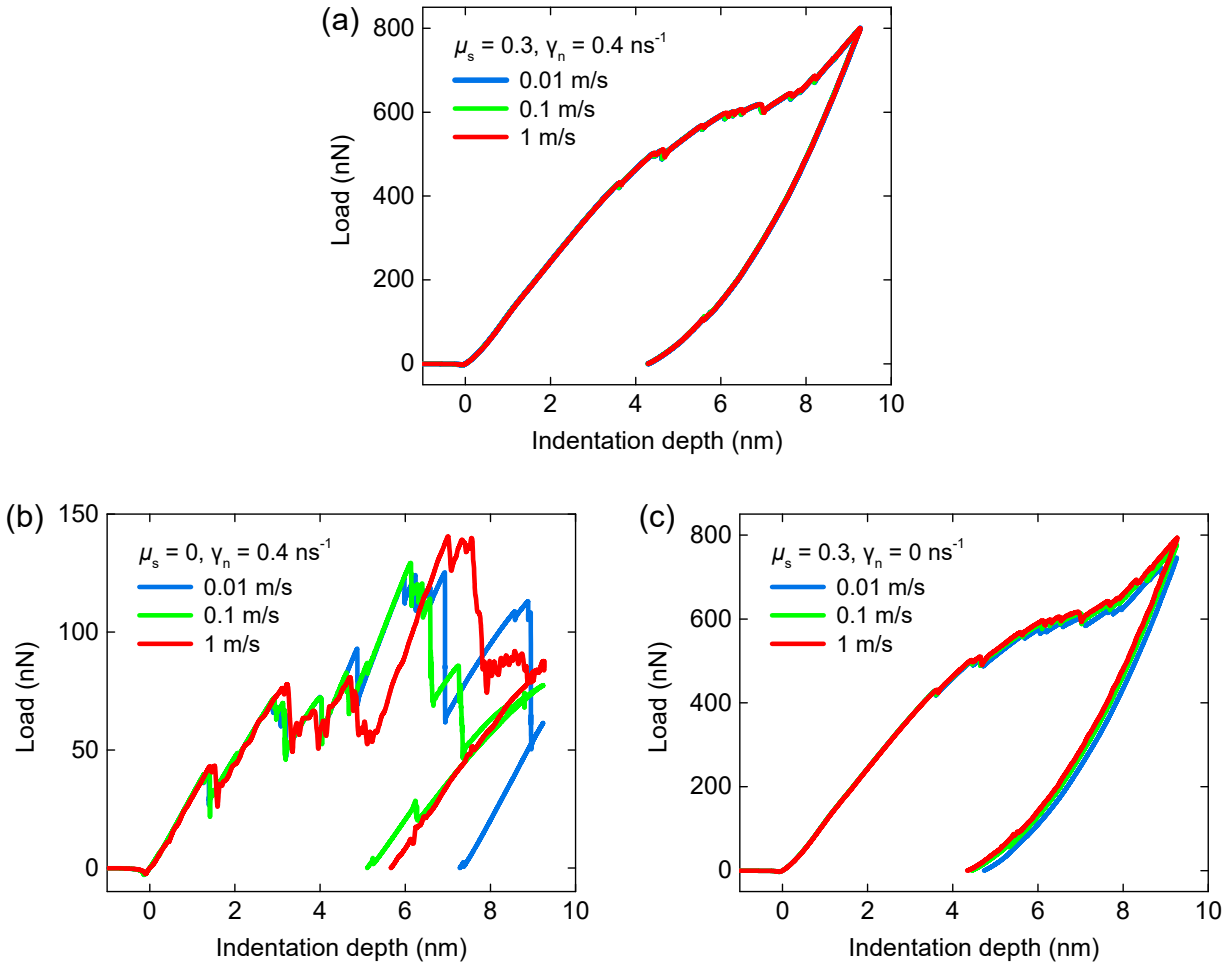

FIG. S11. Simulated load curves for DNPs with various indentation velocities, for different amounts of friction and damping: (a) $\mu_s = 0.3$ and $\gamma_n = 0.4$ ns^{-1}, (b) $\mu_s = 0$ and $\gamma_n = 0.4$ ns^{-1}, (c) $\mu_s = 0.3$ and $\gamma_n = 0$ ns^{-1}. All the simulations have the same initial packing configuration and indent location as those for Fig. 1b in the main text with $w = 7w_0$.

By performing a simulation of collision between two particles with $w = 7w_0$, we determine that the characteristic period of the interparticle collision is on the order of tens of picoseconds. This sets a time scale for considering dynamic elastic effects, so we use a rather high indentation velocity in the indentation simulations with a timestep of 0.5 picosecond to make the computational cost acceptable. Fig. S11 shows the effect of the indentation velocity on the mechanical response of the DNPs. As shown in Fig. S11a, in the presence of friction and interparticle normal viscous damping, the load is insensitive to the indentation velocity change at least for the range of 0.01−1 m/s we have tested. By contrast, the load curves show a dependence on the indentation velocity by forbidding either friction (Fig. S11b) or interparticle normal damping (Fig. S11c). This is because friction together with damping can effectively dissipate the vibrational energy and suppress unimportant excursions in phase space, which makes the mechanical response behave quasi-statically. On the other hand, the absence of friction or damping renders high-frequency vibrations longer-lived. This favors more opportunities to explore phase space in the case of lower indentation velocity.

VII. SUPPORTING TABLES AND FIGURES

TABLE S3. Formulas for the energy calculation listed in Fig. 3 in the main text. The formulas here give the interaction energy change between two particles and their kinetic energy in the current time step, in which $\mathbf{\Delta u}_n$ is the relative normal displacement of two particles in contact in the current step, and I_α is the rotational inertia of particle α. Variables with a superscript of '$n-1$' indicate that they are evaluated in the previous step.

Parameter	Symbol	Formula
Normal elastic energy change	Δe_{ne}	$\mathbf{F}_{ne} \cdot \Delta \mathbf{u}_n$
Normal damping energy change	Δe_{nd}	$\mathbf{F}_{nd} \cdot \Delta \mathbf{u}_n$
Sliding elastic energy change	Δe_{se}	$\frac{1}{2k_s}\mathbf{F}_{se} \cdot \mathbf{F}_{se} - e_{se}^{n-1}$
Sliding plastic energy change	Δe_{sp}	$\mathbf{F}_s \cdot \Delta \mathbf{u}_s + (\mathbf{T}_{si} \cdot \boldsymbol{\omega}_i + \mathbf{T}_{sj} \cdot \boldsymbol{\omega}_j)\,\Delta t - \Delta e_{se}$
Twisting elastic energy change	Δe_{te}	$\frac{1}{2k_t}\mathbf{F}_{te} \cdot \mathbf{F}_{te} - e_{te}^{n-1}$
Twisting plastic energy change	Δe_{tp}	$\mathbf{T}_t \cdot (\boldsymbol{\omega}_i - \boldsymbol{\omega}_j)\,\Delta t - \Delta e_{te}$
Rolling elastic energy change	Δe_{re}	$\frac{a}{2k_r R'}\mathbf{F}_{re} \cdot \mathbf{F}_{re} - e_{re}^{n-1}$
Rolling plastic energy change	Δe_{rp}	$\mathbf{T}_r \cdot (\boldsymbol{\omega}_i - \boldsymbol{\omega}_j)\,\Delta t - \Delta e_{re}$
Translational kinetic energy	ke_{tr}	$\frac{1}{2}\left(m_i \mathbf{v}_i \cdot \mathbf{v}_i + m_j \mathbf{v}_j \cdot \mathbf{v}_j\right)$
Rotational kinetic energy	ke_{rot}	$\frac{1}{2}\left(I_i \boldsymbol{\omega}_i \cdot \boldsymbol{\omega}_i + I_j \boldsymbol{\omega}_j \cdot \boldsymbol{\omega}_j\right)$

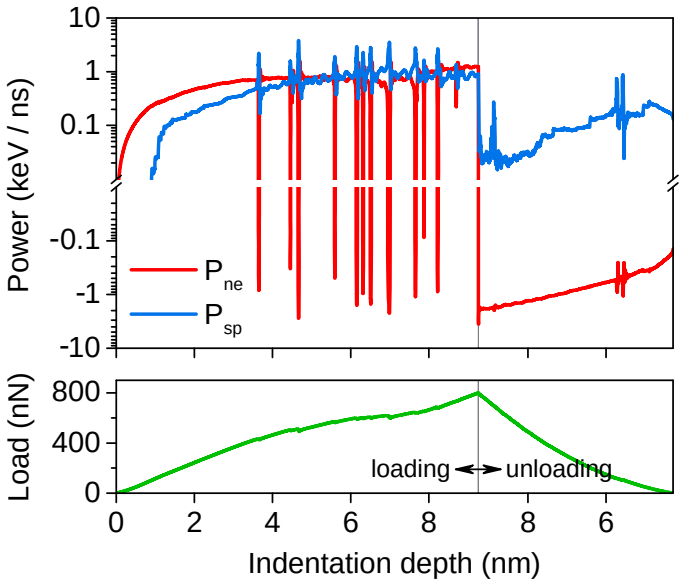

FIG. S12. Power of the normal elastic energy (P_{ne}) and the sliding plastic energy (P_{sp}) for the curve with $\mu_s = 0.3$ and $w = 7w_0$ shown in Fig. 5 in the main text. The corresponding indentation load curve is also depicted for reference. The maximum P_{sp} occurs in the yielding stage, indicating that sliding friction effectively dissipates the interparticle potential energy released during plastic deformation. At the onset of unloading, the magnitude of P_{sp} undergoes a drastic drop, while the magnitude of P_{np} maintains a high level. This demonstrates that sliding friction plays a much less important role than normal elastic contact in determining the mechanical response therein.

VIII. SUPPORTING MOVIES

MOVIE S1. Evolution of the packing configuration over the course of an indentation with the particles colored by their affine von Mises strain, corresponding to Fig. 1 in the main text.

MOVIE S2. Evolution of the interparticle normal contact force chains and the sliding frictional force chains over the course of an indentation with the particles colored by their z-displacement, corresponding to Fig. 4 in the main text.

MOVIE S3. Evolution of the configuration over the course of an indentation of the packing with $\mu_s = 0.3$ and $w = 0.1w_0$, whose indentation load curve is given in Fig. 5c in the main text. The particles are colored by their z-displacement.

MOVIE S4. Evolution of the interparticle normal contact force chains over the course of an indentation of the packing with $\mu_s = 0$ and $w = 7w_0$, whose indentation load curve is given in Fig. 5d in the main text. The particles are colored by their z-displacement.

REFERENCES

[1] A. Munjiza, *The combined finite-discrete element method* (John Wiley & Sons, 2004).
[2] J. Marshall and S. Li, *Adhesive particle flow* (Cambridge University Press, 2014).
[3] K. Johnson, *Contact mechanics* (Cambridge university press, 1985).
[4] K. Johnson, K. Kendall, A. Roberts, and D. Tabor, Surface energy and the contact of elastic solids, Proceedings of the Royal Society of London. A. Mathematical and Physical Sciences **324**, 301 (1971).
[5] B. Derjaguin, V. Muller, and Y. Toporov, Effect of contact deformations on the adhesion of particles, J. Colloid Interface Sci. **53**, 314 (1975).
[6] D. Maugis, Adhesion of spheres: the JKR-DMT transition using a dugdale model, J. Colloid Interface Sci. **150**, 243 (1992).
[7] K. Johnson and J. Greenwood, An adhesion map for the contact of elastic spheres, J. Colloid Interface Sci. **192**, 326 (1997).
[8] R. Sauer and S. Li, A contact mechanics model for quasi-continua, Int. J. Numer. Methods Eng. **71**, 931 (2007).
[9] S. Luding, Cohesive, frictional powders: contact models for tension, Granular Matter **10**, 235 (2008).
[10] C. Thornton, S. Cummins, and P. Cleary, An investigation of the comparative behaviour of alternative contact force models during inelastic collisions, Powder Technol. **233**, 30 (2013).
[11] S. Li, J. Marshall, G. Liu, and Q. Yao, Adhesive particulate flow: the discrete-element method and its application in energy and environmental engineering, Prog. Energy Combust. Sci. **37**, 633 (2011).
[12] S. Plimpton, Fast parallel algorithms for short-range molecular dynamics, J. Comput. Phys. **117**, 1 (1995).
[13] P. Cundall and O. Strack, A discrete numerical model for granular assemblies, Geotechnique **29**, 47 (1979).
[14] J. Israelachvili, *Intermolecular and surface forces* (Elsevier Science, 2011).
[15] R. Ogden, *Non-Linear Elastic Deformations* (Dover Publications, 2013).
[16] W. Callister and D. Rethwisch, *Materials Science and Engineering: An Introduction* (John Wiley & Sons, 2018).
[17] M. Werner, S. Hein, and E. Obermeier, Elastic properties of thin polycrystalline diamond films, Diamond Relat. Mater. **2**, 939 (1993).
[18] Silicon properties, http://www.design.caltech.edu/Research/MEMS/siliconprop.html .
[19] MSC.Marc, https://www.mscsoftware.com/product/marc .
[20] J. Lefever, T. Jacobs, Q. Tam, J. Hor, Y.-R. Huang, D. Lee, and R. Carpick, Heterogeneity in the small-scale deformation behavior of disordered nanoparticle packings, Nano Lett. **16**, 2455 (2016).
[21] C. Thornton, Interparticle sliding in the presence of adhesion, J. Phys. D: Appl. Phys. **24**, 1942 (1991).
[22] C. Thornton and K. Yin, A special volume devoted to the second symposium on advances in particulate technologyimpact of elastic spheres with and without adhesion, Powder Technol. **65**, 153 (1991).
[23] K. Johnson, Mechanics of adhesion, Tribol. Int. **31**, 413 (1998).
[24] B. Derjaguin, Friction and adhesion. iv. the theory of adhesion of small particles, Kolloid Zeits **69**, 155 (1934).
[25] G. Scott, Packing of equal spheres, Nature **188**, 908 (1960).
[26] J. Berryman, Random close packing of hard spheres and disks, Phys. Rev. A **27**, 1053 (1983).
[27] C. Martin and R. Bordia, Influence of adhesion and friction on the geometry of packings of spherical particles, Phys. Rev. E **77**, 031307 (2008).
[28] W. Liu, S. Li, A. Baule, and H. Makse, Adhesive loose packings of small dry particles, Soft Matter **11**, 6492 (2015).